Engineering Structures 251 (2022) 113486

Contents lists available at ScienceDirect

Engineering Structures

journal homepage: www.elsevier.com/locate/engstruct

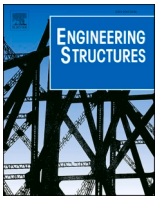

Refined extraction of crack characteristics in large-scale concrete experiments based on digital image correlation

Nicola Gehri *, Jaime Mata-Falcón, Walter Kaufmann

Institute of Structural Engineering, ETH Zürich, Switzerland

ARTICLE INFO

Keywords:
Concrete structures
Experimental measurement
Crack behaviour
Digital image correlation
Image processing
Crack detection
Crack kinematic measurement
Homogeneous testing

ABSTRACT

The accurate extraction of the crack patterns and measurements of crack kinematics are essential for understanding the mechanical behaviour in experiments on structural concrete as well as in the validation and further development of sound mechanical models. This paper presents important refinements of the authors' recently published automatic crack detection and measurement procedure (ACDM) based on surface displacement measurements obtained with digital image correlation (DIC). The proposed refinements are crucial for reliably assessing the crack behaviour in large-scale experiments with complex crack patterns, since the original methods of ACDM may fail or result in biased measurements at locations with closely spaced cracks, crack intersections or cracks with high morphological curvature. The main refinements are (i) a Canny edge-based crack detector, which is applied on the DIC major principal strain field and (ii) enhancements in the crack kinematic measurement to assess the reliability of the results. The latter includes the automatic selection of optimum reference points used in the crack kinematic measurement to increase its reliability and remove uncertain results. The refined ACDM procedure is validated using several large-scale 2.0 × 2.0 m shear panel experiments with highly complex crack patterns. Compared to the original ACDM, significantly thinner cracks can be detected with a much higher reliability of crack locations and crack kinematic measurements, particularly close to crack intersections and at closely spaced cracks. Additionally, two approaches for the statistical consolidation of the large amount of gathered data into characteristic crack properties in large-scale homogeneous concrete element experiments are proposed and compared. The results show that the statistical consolidation of the ACDM data using a 95%-quantile match well with the direct extraction of the best-fit homogeneous crack properties from the full-field DIC displacements. The consolidated data provides highly valuable insight into the mechanical behaviour, especially regarding crack phenomena.

1. Introduction

The knowledge of crack behaviour is crucial for understanding the highly non-linear structural response of concrete. Most mechanical models for concrete walls and shells rely on crack characteristics that consist of the orientation, width, slip and spacing of cracks. These crack characteristics generally vary across the thickness of an element, even under pure in-plane shear loading, e.g. due to the discontinuous nature of the reinforcement. While such variations could theoretically be accounted for [1], mechanical models commonly neglect through-thickness variations [2–7]. Accordingly, direct experimental validation of crack phenomena in these models can be carried out based on crack kinematic measurements on the surface. Novel instrumentation techniques allowing distributed measurement of surface displacements (and strains inside the structure) have recently been developed [8]. They provide detailed information on the specimen's deformation by means of highly accurate measurements of surface displacements with full-field high-resolution digital image correlation (DIC). With this technique, subjective interpretation of measured data is reduced or even avoided compared to conventional technologies where only selective discrete measurements are available [9]. The authors recently presented a procedure for the fully automated detection of crack locations and measurement of crack kinematics from quasi-continuous surface displacement measurement using DIC [10]. In that procedure, called ACDM for "automated crack detection and measurement", the crack pattern is extracted as a skeleton from the major principal strain field using well-established methods from image-processing. At each detected crack location, the crack width and slip are measured by referring to the

* Corresponding author at: Stefano-Franscini-Platz 5, 8093 Zurich, Switzerland.
E-mail address: gehri@ibk.baug.ethz.ch (N. Gehri).

https://doi.org/10.1016/j.engstruct.2021.113486
Received 22 July 2021; Received in revised form 1 October 2021; Accepted 23 October 2021
Available online 9 November 2021

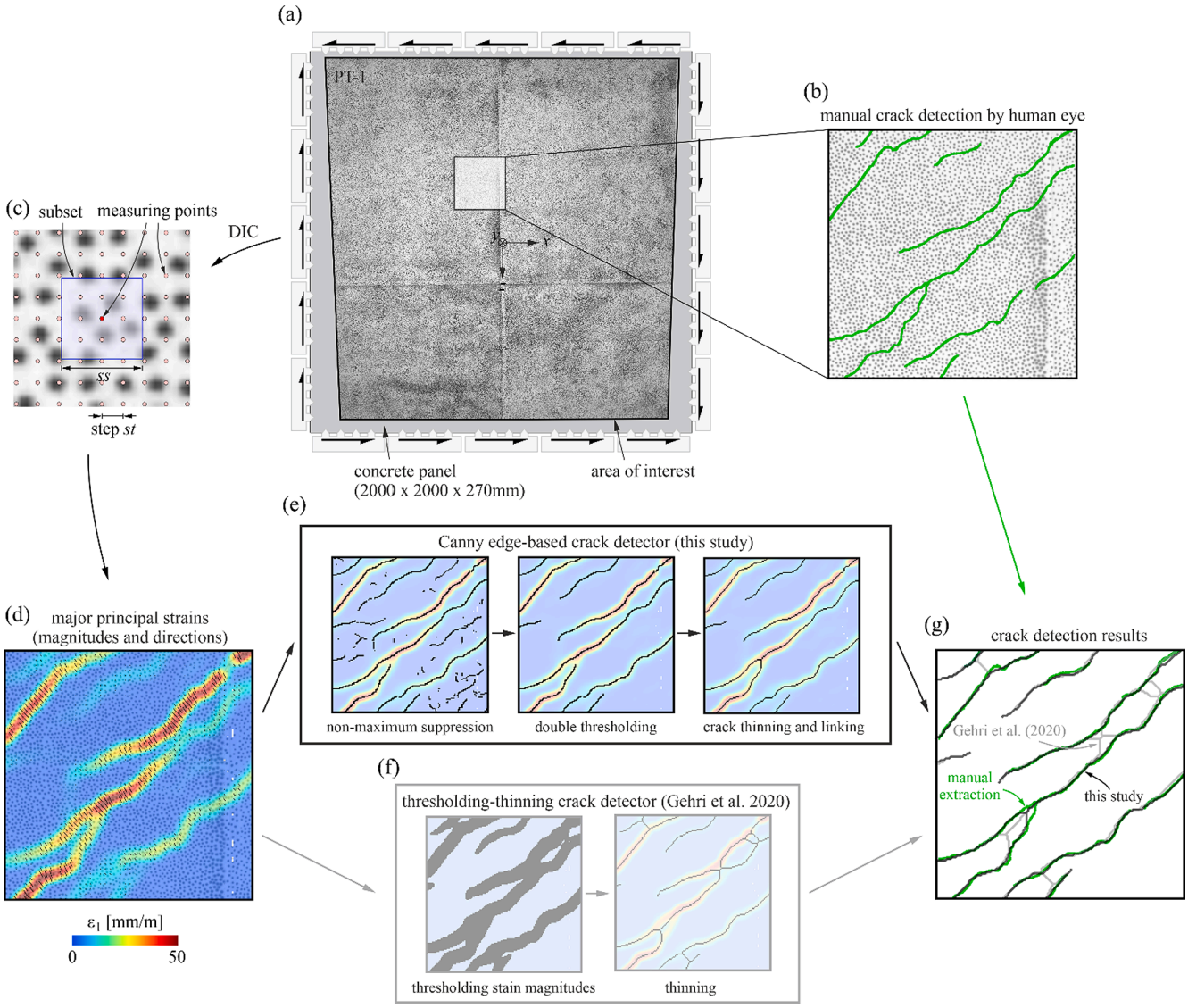

Fig. 1. Concept of the refined crack detection procedure: (a) setup with speckled surface of large-scale Panel Test PT-1 [18] used as test case; (b) window selected to illustrate the details of the crack detector including the "manually" extracted crack pattern (by human eye); (c) DIC definitions; (d) magnitudes (in colour) and directions of the major principal strains; (e) details of the proposed Canny edge-based crack detector applied on DIC results; (f) thresholding-thinning crack detector proposed in [10]; (g) detected cracks compared to the manual extraction as ground truth.

local crack inclination and analysing the local rigid motions of both crack faces. Consequently, the method consistently accounts for local rotations of the specimen (which becomes particularly significant in bending tests, for example). The procedure represents a systematic and fast extraction of the local crack behaviour with high spatial and temporal resolution. The application of the ACDM tool has already led to significant findings in several studies on the mechanical behaviour of structural concrete with conventional and non-conventional reinforcement, such as fibre or textile reinforcement, at the Chair of Concrete Structures and Bridge Design, ETH Zurich [8,11–15] as well as elsewhere [16,17]. However, it has been shown that the method may fail or result in biased measurements in large-scale experiments with a complex crack pattern at locations with closely spaced cracks, crack intersections or cracks with high morphological curvature.

This paper focuses on several important refinements to the original methods of ACDM proposed in [10] regarding an improved crack detector and enhancements in the crack kinematic measurement, which includes the assessment of the measurement reliability. The accurate detection of crack patterns and the reliable measurement of crack kinematic components (width and slip) are crucial, especially when statistically consolidating the detailed data into more understandable characteristic values.

An automated method for acquiring the crack behaviour and the proper statistical evaluation is indispensable in large-scale experiments, where the crack pattern is usually complex and hard to predict. Such experiments form the basis for reliable testing, where the specimen size, reinforcement, static system and loading type are representative of real-life structures. They contribute significant new knowledge of the mechanical behaviour of structural concrete, such as the shear behaviour of girders, which usually cannot be achieved with standard tests [9,11,18]. On the other hand, the evaluation of the crack behaviour in specimens with increased size and higher complexity of the crack pattern requires more effort and advanced instrumentation techniques.

Conventional manual crack measurement techniques, such as the visual inspection by eye, where crack widths are estimated by comparison with printed line widths, demountable mechanical strain gauges

(DEMEC, [19]) or crack loupes, usually fail to capture the crack behaviour in large-scale experiments. They have a highly limited resolution in space and time, are prone to measurement errors and are extremely time-consuming, which can affect the test procedure and also the structural behaviour in cases of loading rate dependencies [10]. Other techniques, such as linear displacement sensors (e.g. LVTDs), active optical tracking systems using markers glued on the concrete surface or image-based crack measurement methods that rely directly on the pixel intensities, affect the test procedure less. Nevertheless, they are either also extremely laborious and only provide spatial discrete information, or limited to cases with wide cracks where no crack slip measurements are required. In many applications, however – especially in experiments that focus on aggregate interlock [11,20–23] – accurate crack slip measurements are of particular relevance and thus indispensable.

DIC counteracts these limitations by providing highly accurate quasi-continuous (in time and space) surface displacement measurements, from which crack locations and full crack kinematics (crack width and slip) can be extracted by applying appropriate methods. In DIC, measuring points – defined as the centre of unique correlation areas called subsets – are tracked by image correlation algorithms (Fig. 1(c)). In many applications, the crack behaviour is still manually extracted from DIC results by visually focusing either on discontinuities in the displacements or on peaks in the major principal strains, and referring to manually defined virtual reference points, which are located at a small distance on opposite sides of the crack at the considered point [24–36]. Such manual procedures are highly time-consuming in large-scale experiments and often lack a consistent and systematic approach, resulting in loss of valuable information and potentially biased interpretations. On the other hand, the few approaches currently available for the systematic and automated detection of crack locations and measurement of crack kinematics, apart from the method refined in this paper, are limited to simple crack patterns with straight, parallel, non-branching cracks [37–39].

The herein proposed refinements of ACDM aim at providing a fully automated tool for the accurate acquisition and evaluation of the crack behaviour in large-scale concrete experiments with complex crack patterns. The concepts and methods are presented using the DIC results of two large-scale 2.0 × 2.0 m concrete panel experiments with orthogonal reinforcement and normal strength concrete, conducted in the Large Universal Shell Element Tester LUSET [18]: PT-1 [18] with a thickness of 0.27 m and rather high amounts of reinforcement ($\rho_x = 2.33\%$ and $\rho_z = 0.86\%$) and SL-1 [11] with a thickness of 0.35 m and light reinforcement ($\rho_x = 0.90\%$ and $\rho_z = 0.22\%$), both loaded in pure in-plane shear. An additional test with smaller dimensions is used for comparison and to demonstrate the general applicability of the proposed methods. This is a tension chord test (CTC-7 [40]) with dimensions measuring 780 × 150 × 150 mm, reinforced with one single reinforcing bar Ø18, subjected to tension. While mechanical models typically assume cracks in panels and tension chords to have a constant opening over their length, the actual crack patterns in the selected tests were complex and included cracks with significant variations of crack width and slip. Hence, the conducted validation covers other loading conditions leading to cracks with variable openings (e.g. bending tests).

The last section of this paper deals with the extraction of characteristic crack properties (width, slip, inclination, spacing) in large-scale concrete element tests, which are homogeneous in terms of loading, boundary conditions, geometry, material and reinforcement (e.g. the shear panels PT-1 and SL-1). Such results are highly relevant as they provide crucial information for understanding the mechanical behaviour and allow a direct model verification. For this purpose, two statistical approaches are proposed:(i) the consolidation of crack information obtained with the refined ACDM, and (ii) the direct extraction of the best-fit homogeneous crack properties from the full-field DIC displacements.

2. Refined automatic crack detection and measurement ACDM

2.1. Overview

The refinements to the automated crack detection and measurement (ACDM) procedure presented in [10] concern neither the overall concept of ACDM nor its processing steps, which can be summarised as follows: The input data of ACDM are the full-field displacement and major principal strain measurements of several measuring stages obtained from digital image correlation (DIC) instrumentation. The crack detection algorithm extracts traceable crack line skeletons in the major principal strain field using the principles of Canny edges [41], either independently for individual measuring stages or for a complete measurement series where the cracks are only detected once. The crack kinematics vectors are computed along the crack paths for each measuring stage based on the local displacements of the crack faces. Finally, they are decomposed into crack widths and slips using the computed local crack inclinations.

The refinements presented in this paper concern the methods of crack detection and crack kinematic calculation, which are outlined in the following sections. In addition, a new approach to compute the measurement reliability in ACDM is derived. These methods allow the accurate and detailed analysis of the crack behaviour in general experiments on brittle materials instrumented with DIC, even in large-scale experiments with a complex crack pattern (consisting of non-uniform branching cracks with intersections, close spacings and high morphological curvatures).

Just like the original ACDM, the entire refined procedure is implemented in an open-source MATLAB tool with a user-friendly graphical user interface (available at: https://gitlab.ethz.ch/ibk-kfm-public/acdm/-/releases/v2.0). The software has been developed to read DIC data generated with the software VIC-2D and VIC-3D from Correlated Solutions Inc. [42]. However, full-field 2D or 3D DIC data from any other processing software can also be used in ACDM, provided that the data are converted to the format of VIC.

2.2. Crack detection

Surface cracks are defined as discontinuities in displacements relative to an initially uncracked state. These displacement discontinuities result in peaks in the strain field with theoretically infinite magnitude. Due to the discrete displacement measurements obtained with DIC, the strains at cracks are finite, with magnitudes related to the crack kinematics. This relationship is used in several studies to detect cracks in experiments that are instrumented with DIC. However, in most cases this is carried out in a manual manner (e.g. [24–36]). Simple automated crack detectors (such as e.g. [37–39]), which extract crack locations from strain magnitudes in one defined direction, fail to capture a crack pattern that consists of cracks with different orientations and opening directions. The detection of general crack patterns thus requires an orientation-independent analysis, which can be achieved by referring to major principal strains and using two-dimensional image-processing techniques. In Fig. 1(e), the major principal strain magnitudes and directions of a small window of the area of interest at the failure load of the large-scale shear panel experiment PT-1 (Fig. 1(a)) are shown. These strains were obtained using a rotationally symmetric centre-weighted Gaussian filter of size 7 to smooth the local strains and reduce the measurement noise. Complete details on the DIC configuration can be found in Appendix C. The use of rather small subset, step and filter sizes has been suggested in order to maintain high spatial resolution [10]. However, it must be considered that this is accompanied by an increased uncertainty in the displacements [8].

The crack detector proposed in [10] represents the first attempt towards an orientation-independent DIC-based crack detection. In this method, high strain areas indicating crack locations are defined by thresholding the magnitudes of the major principal strains (Fig. 1(f)).

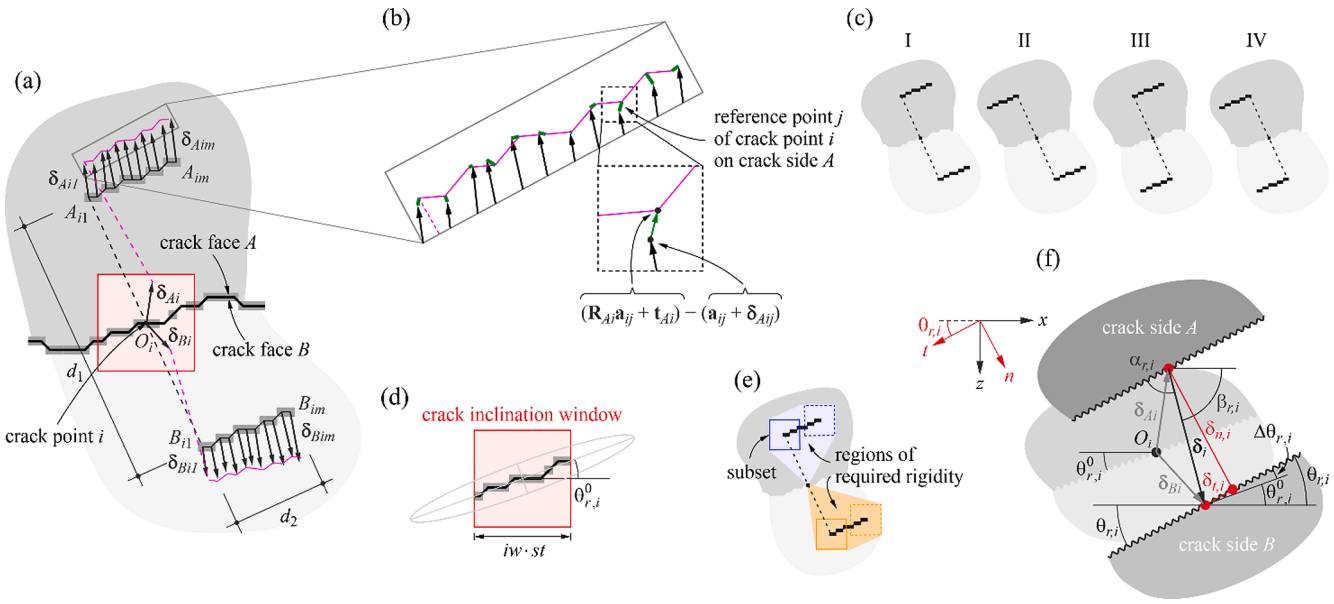

Fig. 2. Details of the refined crack kinematic measurement procedure at crack point *i*: (a) crack face displacements by means of the best-fit rigid displacement of reference points; (b) displacement residuals of the reference points; (c) the four possible setups of the reference points (I-IV) from which the optimum (with smallest residuals) is automatically selected to compute the crack kinematics; (d) definition of the crack inclination in the undeformed state $\theta^0_{r,i}$ (according to Gehri et al. [10]); (e) regions of required rigidity; (f) decomposition of the crack displacement vector $\boldsymbol{\delta}_i$ into crack opening $\delta_{n,i}$ and sliding $\delta_{t,i}$ components (crack width and slip).

The threshold $T_{\varepsilon 1}$ of high strains is chosen to be clearly above the sum of the maximum tensile cracking strain of the material and the measurement uncertainty level. For a given test setup and DIC configuration, the uncertainty of strains is quantified according to the procedure proposed in [8]. For the experiment shown in Fig. 1, the uncertainty of strains is 0.7‰ (see Appendix C) and the threshold of high strains is set to $T_{\varepsilon 1} =$ 4‰ (the maximum tensile cracking strain is approximately 0.2 ‰ [11]). In the next step, the obtained high strain areas are thinned to crack line skeletons using morphological thinning operations. With this crack detector, it was possible to detect a general crack pattern for the first time. However, it has been shown that this approach detects spurious crack locations in areas of closely spaced cracks and crack intersections due to overlapping high strain areas. This phenomenon is shown in Fig. 1(g) by comparing the results to the manually extracted crack locations, where the cracks were marked by thoroughly examining the image section and taking special care whilst defining the cracks. It should be noted that the manual labelling of cracks in images is limited to cracks with a minimum width that is significantly above the smallest detectable crack width of DIC-based crack detectors (usually more than a magnitude [10]). Therefore, the locations of the crack ends differ strongly. Nevertheless, it is recognised that the crack detector fails in many cases when two cracks are close to each other, and poorly predicts the crack branching points. It is also mentioned that lowering $T_{\varepsilon 1}$ would drastically increase the number of undesired spurious cracks. The refined crack detector proposed in this paper improves the original method by taking into account the local variations of strains within the high strain area. Rather than following a thresholding-thinning approach, the procedure directly extracts cracks as ridges in the major principal tensile strain field using the well-established principles of Canny edges [41] (Fig. 1(e)). Ridges are measuring points with strain magnitudes that are maximal compared to the two direct neighbours in the rounded major principal strain directions. Thus, all non-maximum strains are suppressed. Next, all spurious ridges with low strain magnitudes caused by noise are filtered out. This is accomplished by double-thresholding with a user-defined lower ($T_{\varepsilon 1,inf}$) and upper ($T_{\varepsilon 1,sup}$) threshold, where at first all ridges with strain magnitudes below $T_{\varepsilon 1,inf}$ are removed. The remaining ridges are then analysed as entities of connected ridges. Each entity must include at least one ridge point with a strain magnitude greater that $T_{\varepsilon 1,sup}$ in order to be preserved. Otherwise, all ridge points of the entity are removed. Best results were obtained with a lower threshold $T_{\varepsilon 1,inf}$ approximately equal to the sum of the maximum tensile cracking strain of the material and the measurement uncertainty level, and the upper threshold $T_{\varepsilon 1,sup}$ being four times higher. In Fig. 1(e), the thresholds were thus set to $T_{\varepsilon 1,inf} =$ 1‰ and $T_{\varepsilon 1,sup} =$ 4‰. The last step consists of thinning the ridge points into traceable crack lines and linking branches to better represent the physical crack pattern (with many branches being actually linked).

Compared to the thresholding-thinning approach in [10], the herein proposed Canny edge-based crack detector extracts the crack locations much more accurately, especially at crack intersections and in areas of close cracks (Fig. 1(g)). Furthermore, much finer cracks are detected. In Fig. 1, the finest identifiable cracks with the thresholding-thinning approach induce strains of 4‰, whereas the present refined crack detector extracts cracks with four times lower strains. In the particular case shown in Fig. 1, the minimum detectable crack widths are approximately 0.08 px (0.03 mm) for the thresholding-thinning crack detector and 0.02 px (0.007 mm) when applying the Canny edge-based crack detector.

2.3. Crack kinematic measurement

2.3.1. State of the art

The crack kinematic vector describes the relative displacement of the two crack faces. In many existing manual and (semi-)automated methods for extracting crack kinematics from DIC measurements, the crack face displacements are defined using one or several reference points in each crack face's vicinity [10,24–39]. These techniques assume that the regions spanned by the crack face and the reference points (including their DIC subsets) are rigid. This assumption is justified as long as this region is uncracked, as the deformations in uncracked areas of quasi-brittle materials are orders of magnitude smaller than the crack kinematics. It should be mentioned that when using a single reference point on either side of a crack, accurate results are only obtained if the displacements consist of pure translations, since even small rotations bias the crack face displacements significantly [10]. This effect is aggravated by the fact that the reference points cannot be selected too

close to the crack face since DIC displacement measurements near cracks are biased due to intersections of their subsets with the crack itself (see Section 2.3.4). Therefore, in most applications, only approaches that use at least two reference points on each side of the crack and accounts for local rotations of crack faces, such as e.g. [34,36], are applicable.

The first fully automated crack kinematic measurement procedure for DIC results that consistently accounts for local rotations was proposed in [10]. It uses the main principles of the method presented by Campana et al. [43], who developed it for displacement measurements obtained with a DEMEC [19] device on discrete metallic targets glued to the specimen surface. In [10], two reference points on either crack side of a crack point are used to describe the crack lip displacements. The reference points are selected based on the local crack inclination in the undeformed state $\theta^0_{r,i}$, with the first reference point set in a user-defined distance perpendicular to, and the second parallel to $\theta^0_{r,i}$. The crack inclination in the undeformed state $\theta^0_{r,i}$ is defined by means of the major axis of the ellipse that has the same moment of inertia as the undeformed crack part lying within a user-specified window of size *iw* (defined in number of measuring points), with its centre at the particular crack point i (Fig. 2(d)). The positive directions of $\theta^0_{r,i}$ are counterclockwise. The total four reference points used in [10] to compute the crack kinematic vector correspond to A_{i1}, A_{im}, B_{i1} and B_{im} in Fig. 2(a). The first two reference points, A_{i1} and B_{i1}, describe the translations of the particular crack sides, while A_{im} and B_{im} are only used to define (and eliminate) rigid body rotations.

For complex crack patterns, the fundamental assumption of a rigid body for the region spanned by the crack faces and the reference points (including their subsets) that characterise the crack face displacement is often violated [10]. In the following, this region is called the *region of required rigidity* (Fig. 2(e)). On either crack side, it consists of the convex hull of the reference points' subsets and the crack point O_i. Especially in areas with closely spaced cracks or crack intersections, as well as for cracks with high morphological curvature, the *region of required rigidity* is often intersected with cracks, and thus deforms as a non-rigid body. Therefore, the extrapolation of crack face displacements from the reference points may lead to biased values that cannot be filtered due to the lack of information on the measurement reliability. A proper statistical evaluation, however, requires the suppression of biased results. In many analyses, such as the computation of the total crack area, the biased results should be substituted with an estimated value based on available reliable data. The latter process is known as data imputation and is discussed in Section 2.3.5.

2.3.2. New method

In this section, an approach for the crack kinematic measurement at each of a total of n detected crack points is proposed. Besides improving the accuracy of the crack kinematics measurement with respect to existing methods [10,24–32,37–39], the approach allows assessing the reliability of each measuring point. These improvements are achieved by analysing a set of m reference points on both crack sides for each crack point. The reference points are located at a distance $d_1/2$ from the crack. The best-fit rigid body displacements of the set of reference points are computed, and the crack face displacements are extrapolated from these (Fig. 2(a)).

Analogously to the original method in [10], the reference points on both crack sides A and B of crack point i, $A_{i1},\ldots,A_{im}$ and $B_{i1},\ldots B_{im}$, are selected among the available grid of measuring points according to the local crack inclination in the undeformed state $\theta^0_{r,i}$ (see Section 2.3.1). A_{i1} and B_{i1} are set perpendicular to $\theta^0_{r,i}$ at a distance $d_1/2$ from the location of the crack point O_i. The remaining reference points trace the gridded line parallel to $\theta^0_{r,i}$ with length d_2 on both crack sides (Fig. 2(a)).

In the following, the computation of the crack face displacement for crack side A is described. Note that the same applies to crack side B by replacing the corresponding variables and indices in the formulas. The best-fit rigid in-plane motion of the set of m reference points at crack point i consists of a rotation matrix $\mathbf{R}_{Ai}$ that rotates the points in the surface plane (xz) through the angle φ_{Ai} about the origin, and a translation vector $\mathbf{t}_{Ai}$ translating the same points:

$$\mathbf{R}_{Ai}=\begin{bmatrix}\cos(\varphi_{Ai}) & -\sin(\varphi_{Ai})\\ \sin(\varphi_{Ai}) & \cos(\varphi_{Ai})\end{bmatrix},\quad \mathbf{t}_{Ai}=\begin{bmatrix}t_{Ai,x}\\ t_{Ai,z}\end{bmatrix} \tag{1}$$

such that the sum of the residuals between the true and the best-fit rigid displacements of the reference points is minimised (Fig. 2(b)):

$$(\mathbf{R}_{Ai},\mathbf{t}_{Ai})=\underset{\mathbf{R}_{Ai}\in SO(2),\mathbf{t}_{Ai}\in\mathbb{R}^2}{\operatorname{argmin}}\sum_{j=1}^{m}w_{Aij}\left\|\left(\mathbf{R}_{Ai}\mathbf{a}_{ij}+\mathbf{t}_{Ai}\right)-\left(\mathbf{a}_{ij}+\boldsymbol{\delta}_{Aij}\right)\right\|^2 \tag{2}$$

In Eq. (2)[1], $\mathbf{a}_{ij}$ are the in-plane position of the reference points in the undeformed state and $\boldsymbol{\delta}_{Aij}$ the corresponding displacement vectors. w_{Aij} denote the weights of the reference points. In the following, the weights are inversely proportional to the distance from the crack point i to the reference points: $w_{Aij}=\left\|\mathbf{o}_i-\mathbf{a}_{ij}\right\|^{-1}$. However, more advanced weights could easily be implemented, which, for example, could take into account the uncertainty of the subset correlation at the reference points (and thus the uncertainty of $\boldsymbol{\delta}_{Aij}$). The term $\left(\mathbf{R}_{Ai}\mathbf{a}_{ij}+\mathbf{t}_{Ai}\right)$ in Eq. (2) denotes the position of reference point j after applying the best-fit rigid transformation, whereas $\left(\mathbf{a}_{ij}+\boldsymbol{\delta}_{Aij}\right)$ describes the measured position in the deformed state (Fig. 2(b)). The solution of Eq. (2), which provides the optimum rotation $\mathbf{R}_{Ai}$ and translation $\mathbf{t}_{Ai}$, is obtained with the method presented in [44], with its steps being summarised in Appendix A.

The crack face displacement $\boldsymbol{\delta}_{Ai}$ is extrapolated from the best-fit rigid body displacement of the reference points:

$$\boldsymbol{\delta}_{Ai}=\left(\mathbf{R}_{Ai}\mathbf{o}_i+\mathbf{t}_{Ai}\right)-\mathbf{o}_i \tag{3}$$

where $\mathbf{o}_i$ is the position of the crack point i in the undeformed state. However, Eq. (3) can only reliably be used to compute crack face displacements if it is ensured that the *region of required rigidity* does not deform. A procedure to assess the deformations in the *region of required rigidity*, and thus the reliability of the computed crack face displacement, is proposed in Section 2.3.3.

The crack kinematic vector $\boldsymbol{\delta}_i$ at crack point i (describing the relative crack face displacement from crack side A to B) results in:

$$\boldsymbol{\delta}_i=\boldsymbol{\delta}_{Bi}-\boldsymbol{\delta}_{Ai} \tag{4}$$

In many applications, and particularly in most large-scale experiments, the assessment of the crack behaviour requires the accurate decomposition of the crack kinematic vector into crack opening and sliding components (perpendicular and parallel to the crack inclination, commonly referred to as crack width and slip, respectively). As mentioned above, many mechanical models, especially on aggregate interlock (e.g. [21,45,46]) react highly sensitive to even small changes in these components.

Therefore, it is essential to account for local rotations of the specimen during the test. The local crack inclination at crack point i in the deformed state is defined as

$$\theta_{r,i}=\theta^0_{r,i}-\varphi_i \tag{5}$$

where $\theta^0_{r,i}$ denotes the crack inclination in the undeformed state, being a property of the local shape of the crack line (see Section 2.3.1), and φ_i the mean rotation of the two crack faces:

[1] The expression $SO(2)$ stands for *special orthogonal group* in 2 dimensions, which consists of 2×2 orthogonal matrices of determinant 1. This is the group of 2-dimensional rotation matrices.

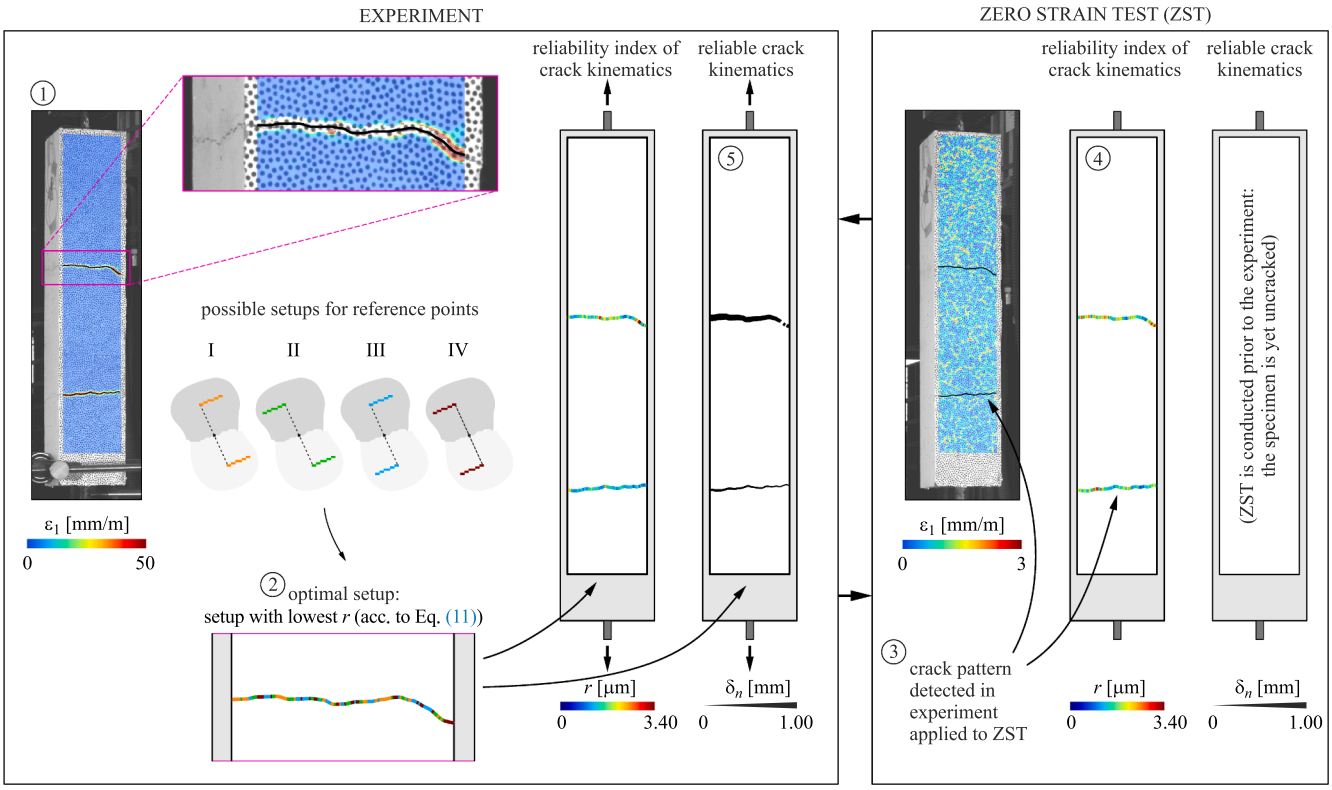

Fig. 3. Details of the reliability measurement of the crack kinematics by means of tension test CTC-7 [40]: 1. Detecting cracks in the experiment at a measuring stage with the fully developed crack pattern; 2. Selecting the optimal setup of reference points; 3. Applying the crack pattern and the optimal setup of reference points to a characteristic measuring stage of the Zero Strain Test (ZST – conducted prior to the experiment, where the yet uncracked specimen is moved in space without applying any load); 4. Measuring the reliability indices of the crack kinematics at the ZST; 5. Setting the threshold of accepted uncertainty of the crack kinematic measurement to $T_r = 2r_{RMS,ZST}$ and removing crack kinematic measurements with $r_i > T_r$ in the experiment.

$$\varphi_i = \frac{\varphi_{Ai} + \varphi_{Bi}}{2} \tag{6}$$

with φ_{Ai} and φ_{Bi} being obtained from Eq. (1). Note that the minus sign in Eq. (5) results from opposite positive directions between crack inclinations (counterclockwise) and crack face rotations (clockwise), as shown in Fig. 2(f). The crack opening ($\delta_{n,i}$) and sliding ($\delta_{t,i}$) components of $\boldsymbol{\delta}_i$ are obtained by means of the following transformation matrix:

$$\mathbf{Q}_{nt,i} = \begin{bmatrix} \sin(\theta_{r,i}) & \cos(\theta_{r,i}) \\ -\cos(\theta_{r,i}) & \sin(\theta_{r,i}) \end{bmatrix} \tag{7}$$

with:

$$\begin{bmatrix} \delta_{n,i} \\ \delta_{t,i} \end{bmatrix} = \mathbf{Q}_{nt,i}\boldsymbol{\delta}_i \tag{8}$$

The reader is referred to Fig. 2(f) for details of the decomposition of the crack kinematic vector $\boldsymbol{\delta}_i$. The steps in Eqs. (2)–(8) are repeated for each of the n detected crack points at all examined measuring stages, resulting in a complete analysis of the crack behaviour of an experiment. Compared to the original method proposed in [10] with only two reference points on each crack side, the present procedure provides more accurate crack kinematic measurements, with the crucial advantage that the residuals between the true and the best-fit rigid displacements of the reference points in Eq. (2) allow the assessment of the reliability of each measurement.

2.3.3. *Reliability and optimum setup of reference points*

As stated in Section 2.3.1, the reliability of crack kinematic measurements depends on the deformations of the *regions of required rigidity* on both crack sides (Fig. 2(e)). The less these regions deform (i.e., the more rigid they are), the higher are the reliabilities of the crack face displacement measurements and consequently of the crack kinematics. However, due to the inevitable need to determine the crack face displacement via reference points (displacement measurements directly at the crack faces are biased since the DIC subsets of such measuring points are intersected by the crack), the actual deformations cannot be assessed within the entire *region of required rigidity*. This means that the reliability of the crack kinematics measurement can only be approximated. In the presented approach, the deformation of the *region of required rigidity* is approximated by analysing the residuals between the true and the best-fit rigid displacements of reference points obtained from Eq. (2) (the residuals are indicated in green in Fig. 2(b)). However, the following must be considered when using this approach: Assume that a close parallel second crack exists between the examined crack shown in Fig. 2(e) and the set of its reference points on one of the crack sides. This second crack would lead to deformations in the *region of required rigidity* that the proposed method will not detect but will end up being added to the actual crack kinematic measurement (the degree of the bias depends on the kinematics of this second crack). Hence, in such particular cases, the estimation of the reliability would fail in detecting biased measurement. This phenomenon, however, can be avoided by setting the distances d_1 small enough such that the subsets of the reference points just do not intersect the crack, ensuring that the reference points still contain undistorted displacement measurements. Hence, a very close second crack between the examined crack and its set of reference points would then intersect the subsets of the reference points, thus leading to significant residuals. Therefore, the approximation of the crack face displacement reliability through the residuals of the reference points is reliable when using an appropriate distance d_1 (discussed in Section 2.3.4).

In the following, the details of the approach to quantify the reliability

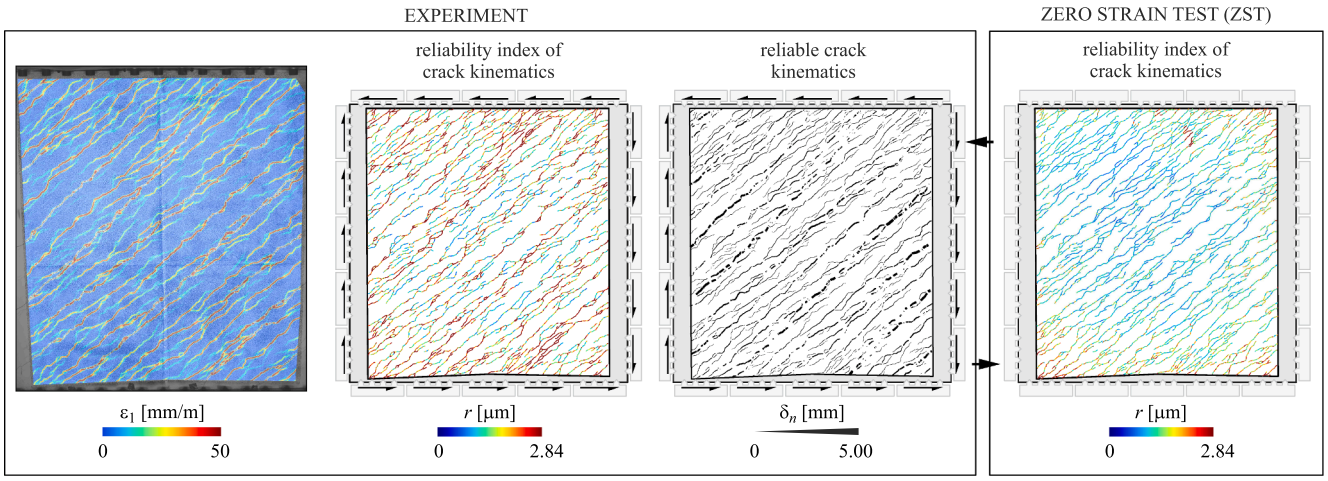

Fig. 4. Results of the reliablity measurement of the crack kinematics in large-scale pure shear test PT-1 [18]: After optimisation of the setup of reference points, crack kinematic measurements with $r_i > T_r = 2r_{RMS,ZST}$ are classified to be unreliable and removed.

of the crack kinematic measurements using the residuals in Eq. (2) is presented. The residuals r_{Aij} and r_{Bij} denote the differences between the best-fit rigid and the true displacements for reference point j on the two crack sides of crack point i:

$$r_{Aij} = \left\| \left(\mathbf{R}_{Ai}\mathbf{a}_{ij} + \mathbf{t}_{Ai} \right) - \left(\mathbf{a}_{ij} + \boldsymbol{\delta}_{Aij} \right) \right\|$$
$$r_{Bij} = \left\| \left(\mathbf{R}_{Bi}\mathbf{b}_{ij} + \mathbf{t}_{Bi} \right) - \left(\mathbf{b}_{ij} + \boldsymbol{\delta}_{Bij} \right) \right\| \quad (9)$$

The deformations of the sets of reference points are expressed by the weighted root mean square (RMS):

$$r_{Ai} = \sqrt{\frac{\sum_{j=1}^{m} w_{Aij} r_{Aij}^2}{\sum_{j=1}^{m} w_{Aij}}}, \quad r_{Bi} = \sqrt{\frac{\sum_{j=1}^{m} w_{Bij} r_{Bij}^2}{\sum_{j=1}^{m} w_{Bij}}} \quad (10)$$

where the weights w_{Aij} and w_{Bij} corresponds to those used in Eq. (2). Finally, the crack kinematic measurement reliability at crack points i is expressed with the following reliability index r_i:

$$r_i = \sqrt{\frac{r_{Ai}^2 + r_{Bi}^2}{2}} \quad (11)$$

where a small value of r_i indicates a high reliability of the crack kinematic measurement $\boldsymbol{\delta}_i$ and vice versa.

Compared to the original method proposed in [10], where a fixed setup of reference points is used, the present approach now allows optimising the setup of reference points (Fig. 2(c)). In each measuring stage and at each crack point i, the setup with lowest r_i is selected for computing the crack kinematics.

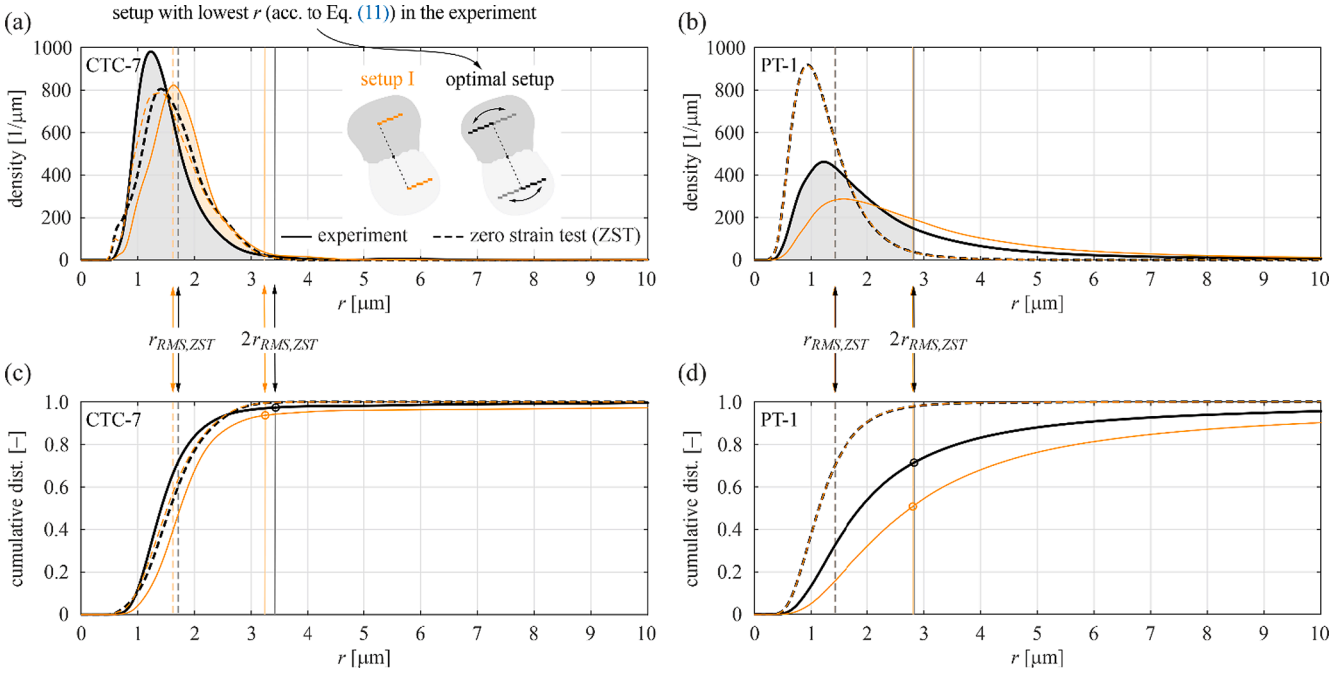

Fig. 5. Distribution of reliability index r (according to Eq. (11)) at ultimate load of CTC-7 and PT-1: (a) and (b) kernel density estimation for the fixed setup of reference points "I"(used in the original ACDM) and the optimum setup with a bandwidth of 0.1 mm; (c) and (d) corresponding cumulative distribution function. $r_{RMS,ZST}$ denotes the root mean square (RMS) of the reliability indices of all cracks points (see Eq. (12)) applied to the zeros strain test (ZST) and by using the optimum setup.

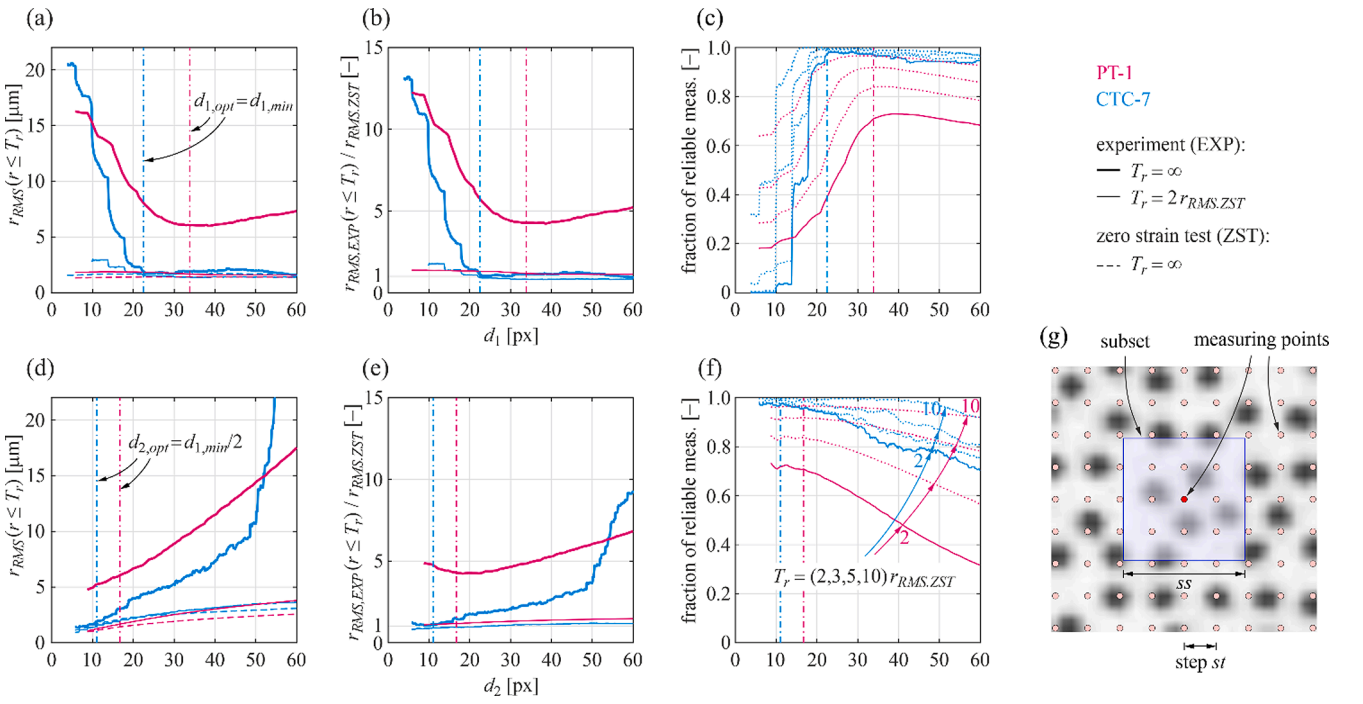

Fig. 6. Influence of distances d_1 (upper row) and d_2 (lower row) used for the crack kinematic measurement (see definitions in Fig. 2(a)) on the total reliability of the crack kinematic measurement: (a) and (d) influence on the root mean square of all reliability indices smaller than the threshold of accepted uncertainty $r_{RMS,EXP}(r \leqslant T_r)$; (b) and (e) influence on the reliabilities of the experiment normalised with those of the ZST $r_{RMS,EXP}(r \leqslant T_r)/r_{RMS,ZST}$; (c) and (f) influence on the ratio of reliable measurements using different thresholds of accepted uncertainty T_r; (g) DIC definitions.

Besides optimising the setup of reference points, the second benefit of measuring the reliability of the crack kinematics is to allow a proper statistical analysis of the crack behaviour (see Section 3.2) by removing uncertain results. In the present approach, a crack kinematic measurement is removed if the reliability index r_i exceeds a user-defined threshold T_r. The threshold should be above the measurement uncertainty but small enough to identify biased crack kinematic measurements. The DIC uncertainty is typically measured by conducting a Zero Strain Test (ZST) prior to the experiment, where the yet uncracked specimen is moved in space without applying any load [8]. In Fig. 3 and Fig. 4, the process of evaluating the uncertainty of the crack kinematic measurement and their usage in defining the threshold of accepted uncertainty T_r is shown. Fig. 3 shows the details of the process for a very simple crack pattern in CTC-7, whereas in Fig. 4, the main steps are shown for the complex crack pattern obtained in PT-1. The crack locations and the optimum setup of reference points are obtained from the experiment at a measuring stage with the fully developed crack pattern. They are applied to a characteristic measuring stage of the ZST, where the reliability indices of the crack kinematic measurements $r_{i,ZST}$ at these fictitious cracks are extracted. The proposed threshold of accepted uncertainty T_r refers to the root mean square (RMS) of the reliability indices of all crack points:

$$r_{RMS} = \sqrt{\frac{\sum_{i=1}^{n} r_i^2}{n}} \tag{12}$$

where in the following, the threshold is set to $T_r = 2r_{RMS,ZST}$ by using Eq. (12) with $r_i = r_{i,ZST}$. These thresholds are $T_r = 3.40\ \mu$m in CTC-7(Fig. 3) and $T_r = 2.84\ \mu$m in PT-1(Fig. 4), and correspond to the 99.6% and 97.0%-quantiles of the reliability indices in the ZST, respectively (see also Appendix C). In the experiments, all crack kinematic measurements with $r_i > T_r$ are classified to be unreliable and removed.

By comparing the experiments CTC-7(Fig. 3) and PT-1(Fig. 4), it is shown that the latter experiment contains much more unreliable crack kinematic measurements that have been removed. Quantitatively, this is shown in Fig. 5, where the distributions of the reliability index r are plotted. The two markers in Fig. 5(c) and (d) indicate the ratios of reliable crack kinematic measurements in the experiments when applying $T_r = 2r_{RMS,ZST}$. Although the crack kinematics measurement uncertainty in both experiments is similar (in CTC-7: $r_{RMS,ZST} = 1.7\mu$m and in PT-1: $r_{RMS,ZST} = 1.4\mu$m), 97.4% of all measurements are classified to be reliable in CTC-7, while this ratio is only 70.9% in PT-1. This difference is simply explained by the much higher complexity of the crack pattern in PT-1. A summary of the key values of the crack kinematic measurement reliability assessment is given in Appendix C.

Additionally, the relevance of optimising the setup of reference points used in the measurement of the crack kinematics is studied in Fig. 5. It is shown that by optimising the setup from the four possible arrangements of the reference points (Fig. 2(c), the crack kinematic measurement reliability is significantly increased compared to a fixed setup. In orange colour, the results are shown for the fixed setup "I", which was used in the original ACMD [10]. The results for setups "II" to "IV" are very similar to the ones with setup "I" and are thus not displayed in Fig. 5. Note also that the setup of reference points has only marginal influence on the reliability indices of the Zero Strain Test (ZST) $r_{i,ZST}$ (dashed lines), what explains the similar values of $r_{RMS,ZST}$ between setup "I" and the optimised setup. By keeping the reference points constant in setup "I", only slightly more than half of the measurements (50.8%) are below the set reliability threshold, whereas by optimising the setup – as already mentioned – 70.9% of all measurements are classified as reliable. Analogously, by optimising the setup in CTC-7, the ratio of reliable measurements is increased from 93.6% to 97.4%. In conclusion, the proposed method to optimise the setup of reference points significantly improves the measurement reliability, especially in complex crack patterns.

2.3.4. Parameter optimisation

This section deals with the optimisation of the two remaining parameters in the crack kinematic measurement procedure: the distances

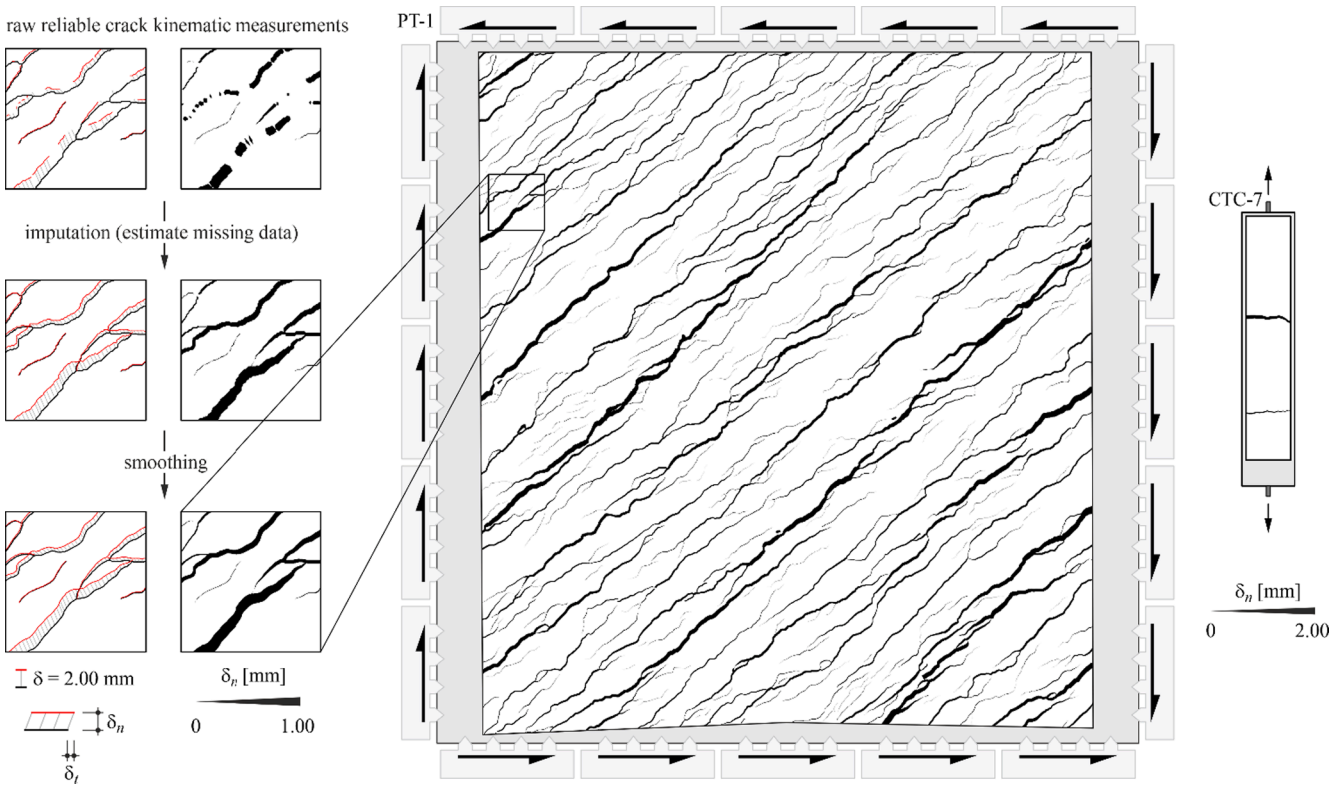

Fig. 7. Complete smoothed crack patterns with crack opening measurements indicated by line width for PT-1 and CTC-7. For measurements with $r > T_r = 2r_{RMS,ZST}$, the crack kinematics were imputed based on neighbouring reliable data.

d_1 and d_2 (Fig. 2(a)). The distance d_2 determines the number of reference points m used to measure the crack face displacement, while d_1 defines their distance from the crack line. Fig. 6 shows the parameter studies of d_1 and d_2, respectively, where their sensitivity on the reliability of the crack kinematic measurements is analysed. For this purpose, the two experiments and their ZST in Fig. 3 and Fig. 4 are examined. In Fig. 6(a)-(c), the distance d_2 is kept at its optimum ($d_2 = d_{2,opt}$); in Fig. 6(d)-(f) same applies to distance d_1 ($d_1 = d_{1,opt}$). The other parameter is varied in each case. The optimum distances $d_{1,opt}$ and $d_{2,opt}$ are discussed in more detail below.

The total reliability of a given configuration of d_1 and d_2 is expressed by the root mean square of all reliability indices smaller than the threshold of accepted uncertainty T_r:

$$r_{RMS}(r \leqslant T_r) = \sqrt{\frac{\sum_{i=1}^{n} r_i^2 [r_i \leqslant T_r]}{\sum_{i=1}^{n} [r_i \leqslant T_r]}} \tag{13}$$

Note that setting $T_r = \infty$ in Eq. (13) will lead to Eq. (12), i.e. $r_{RMS}(r \leqslant \infty) = r_{RMS}$. Fig. 6(a) and (d) show the influence of d_1 and d_2 on the absolute values of $r_{RMS}(r \leqslant T_r)$ for the experiment (labelled EXP) and the ZST, respectively. In Fig. 6(b) and (e), the reliabilities of the experiment are normalised with the ones from the ZST to account for the change in the DIC uncertainty when varying d_1 and d_2. Here, the DIC uncertainty is expressed by the total reliability of the crack kinematics in the ZST ($r_{RMS,ZST}$, see dashed lines in Fig. 6). Note that only a change in the distance d_2 affects the $r_{RMS,ZST}$. This is explained by the source of errors in the DIC measurement. Mata-Falcón et al. [8] showed that systematic errors (bias) caused by imperfections in the optical system model (due to insufficiently accurate calibration, ambient conditions with changing temperature or airflow causing Schlieren effect, etc.) typically dominate random errors (noise). Since the bias is similar between nearby points and tends to cancel out in relative displacement measurements within small areas, an increased distance d_2 leads to a higher bias and thus to an increased $r_{RMS,ZST}$. In Fig. 6(c) and (f), the ratio of reliable measurements using different thresholds of accepted uncertainty T_r is shown.

The optimum distances $d_{1,opt}$ and $d_{2,opt}$ are extracted at the minima of $r_{RMS,EXP}(r \leqslant T_r)/r_{RMS,ZST}$ for the case $T_r = \infty$ (see thick lines in Fig. 6(b) and (e)). This approximately corresponds to the maximum ratios of reliable measurements in Fig. 6(c) and (f). Note that for very small d_1, the subsets of the reference points are intersected with the examined crack, which leads to high biases and thus to low total reliabilities (corresponds to high values of $r_{RMS,EXP}(r \leqslant T_r)$, see Fig. 6(a) and (b)). The smallest distance $d_{1,min}$ that just does not lead to subsets being intersected with the examined crack can be determined analytically. For this purpose, the critical case of a 45° inclined crack with respect to the edges of the subset is considered, leading to the following formula:

$$d_{1,min} = \sqrt{2}\left\lceil \frac{ss+1}{st} \right\rceil st \tag{14}$$

where ss denotes the subset size and st the step between two measuring points, both in pixels (Fig. 6(g)). The ceiling function is used to account for the grid of available measuring points. From Fig. 6(b), it is noticed that the optimum value $d_{1,opt}$ coincides with $d_{1,min}$ ($d_{1,opt} = d_{1,min}$). Higher values of d_1 again decrease the total reliability of the crack kinematic measurement (corresponds to an increase of $r_{RMS,EXP}$), since the subsets of the reference points have a higher probability of intersecting adjacent cracks. It also must be considered that – as stated in Section 2.3.3 – rather small values of d_1 are to be preferred in order to minimise the risk of non-detectable measurement biases caused by close parallel cracks. The optimum distance of d_2 has empirically been found to be approximately at $d_{2,opt} \approx d_{1,min}/2$ by referring to Fig. 6(e). In all further analyses, the proposed optimum parameters $d_{1,opt}$ and $d_{2,opt}$ are used.

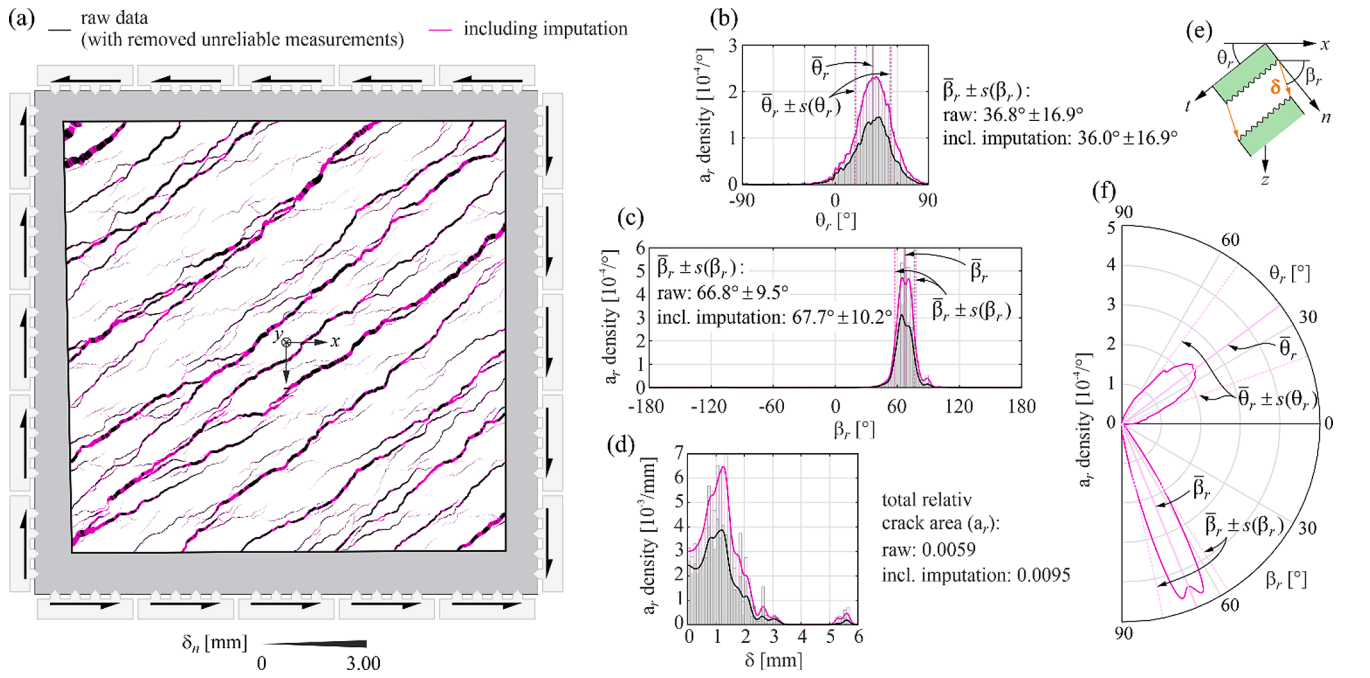

Fig. 8. Statistical analysis of crack characteristics from ACDM data applied to the homogeneous structural element experiment SL-1 [11] (reliable raw ACDM data are indicated in black; data including imputed crack kinematics in magenta): (a) crack pattern with crack opening measurements indicated by line width; (b) and (c) relative crack area density estimations, mean values and angular deviations of the crack inclination θ_r and the crack kinematic vector direction β_r; (d) relative crack area density estimations of crack kinematic vector magnitudes δ; (e) notation of crack characteristics; (f) polar representation of the statistics of θ_r and β_r for the data including imputed crack kinematics.

2.3.5. *Data imputation*

Removing biased crack kinematic measurements is crucial for the statistical evaluation of the data. In Section 2.3.3, a method for the identification and rejection of crack kinematic measurements with low reliabilities has been proposed. In many applications, imputation of the removed data (i.e. the best substitution with an estimated value based on available reliable data) is required. This applies in particular to the computation of the total crack area, but also to any analysis that relies on the distribution of the crack kinematics. In Fig. 7, the crack patterns with imputed crack kinematics for measurements where $r > T_r = 2r_{RMS,ZST}$ are shown. In these plots, the line thicknesses correspond to the crack widths. The crack kinematics are imputed using the method proposed in [10], where missing values are estimated by linear interpolation of neighbouring reliable measurements of the particular cracks branch. While the quantification of the reliability of imputed data is out of the scope of this paper, a reasonable approach to maximise the reliability is to impute the crack kinematic vector (rather than simply the corresponding crack width and slip components). Thereby, it is implicitly assumed that the crack faces remain rigid and displace uniformly between the point used for the imputation and the one whose crack kinematics are substituted. Additionally, the crack lines and the crack kinematic results are smoothed, yet only for visualisation purposes (according to the method described in [10]). Note that for further data processing steps, such as the statistical consolidation in Section 3.2, unsmoothed results are used.

3. Characteristic crack behaviour in large-scale homogeneous element tests

3.1. *Relevance*

Due to the highly non-linear behaviour of concrete, the investigation of the actual load-deformation behaviour requires experiments that are representative of real-life structures. In many applications, especially in the experimental testing of concrete slabs and shell structures, large-scale experiments with a representative static system and loading type can contribute significant new knowledge. Their relevance is widely accepted in the research community, particularly for structures not complying with the prerequisites of limit analysis methods, which applies to many existing structures and most applications of non-conventional reinforcements, such as fibre or textile reinforcement [18].

The recently developed Large Universal Shell Element Tester (LUSET) at ETH Zurich [18] allows for the testing of representative large-scale concrete elements subjected to general loads. In its standard configuration, the shell element is homogeneously loaded. In addition, the tested element is typically homogeneous in terms of its geometry, material and reinforcement. Under these conditions, the structural behaviour is homogeneous, allowing direct validation of established mechanical models. Generally, the latter rely on the fundamental assumption of homogeneous cracks (i.e. one set of straight parallel cracks with uniform spacing, opening direction and magnitude, e.g. [4–7]). Hence, characteristic values of crack properties (width, slip, inclination, spacing) consolidated from the ACDM data provide highly valuable information for the development and validation of such models. The investigation of possible multiple dominant sets of cracks is therefore not addressed in this study.

In the following, a procedure for the statistical consolidation of the results obtained with the refined ACDM is proposed. Additionally, the direct extraction of the best-fit homogeneous crack characteristics from the full-field DIC displacements is presented. The latter approach directly relies on the DIC displacement measurement, without the need to process the data with ACDM first. The two approaches are compared using the results from the large-scale pure shear element experiment SL-1 [11], tested in LUSET. The experiment exhibited a complex crack pattern with dominating diagonal cracks opening non-orthogonally. With these properties, the experiment allows evaluating and comparing the validity of the two proposed approaches.

3.2. Statistical consolidation of ACDM results

The proposed statistical consolidation of crack properties obtained with the refined ACDM aims at providing characteristic values of crack width, slip, inclination and spacing of a tested homogeneous structural element. Since the crack width and slip are coupled by the crack inclination, the crack kinematic vector magnitudes δ and their directions β_r are analysed instead. Due to the directional nature of the crack inclination and the crack kinematic vector direction, circular statistics is applied to these data. Their characteristic values are expressed in terms of the weighted mean angles. On the other hand, the extraction of characteristic crack kinematic magnitudes and crack spacings is more difficult. This particularly applies to complex crack patterns, where it is difficult to consolidate ACDM data into characteristic values that adequately represent the mechanical behaviour. Thus, an empirical approach for their statistical consolidation based on calibrated quantiles is shown in Section 3.4.

In the following, the analysis of the weighted mean crack inclination and crack kinematic vector direction is presented. The measurements at each crack point are weighted by the local crack area associated with the crack measuring point to account for the assumption that the crack behaviour is primarily governed by larger cracks. Hence, the weights are defined as:

$$w_i = \delta_i l_i \tag{15}$$

where δ_i is the crack kinematic vector magnitude and l_i the crack line segment length at crack point i. The weighted mean crack inclination $\bar{\theta}_r$ and crack kinematic vector direction $\bar{\beta}_r$ are then computed using the cartesian coordinates of the mean vectors and weights according to Eq. (15):

$$X_{\theta_r} = \frac{\sum_{i=1}^{n} w_i \cos(2\theta_{r,i})}{\sum_{i=1}^{n} w_i}, \quad Y_{\theta_r} = \frac{\sum_{i=1}^{n} w_i \sin(2\theta_{r,i})}{\sum_{i=1}^{n} w_i}$$
$$X_{\beta_r} = \frac{\sum_{i=1}^{n} w_i \cos(\beta_{r,i})}{\sum_{i=1}^{n} w_i}, \quad Y_{\beta_r} = \frac{\sum_{i=1}^{n} w_i \sin(\beta_{r,i})}{\sum_{i=1}^{n} w_i} \tag{16}$$

leading to the weighted mean angles:

$$\tan\left(2\bar{\theta}_r\right) = \frac{Y_{\theta_r}}{X_{\theta_r}}$$
$$\tan\left(\bar{\beta}_r\right) = \frac{Y_{\beta_r}}{X_{\beta_r}} \tag{17}$$

The procedure for computing mean angles is shown e.g. in [47]. Note that the factor of 2 in Eq. (16) is due to the axial (diametrically bimodal) nature of the crack inclination ($\bar{\theta}_r \in (-90°, 90°]$). The quantities:

$$\rho_{\theta_r} = \sqrt{X_{\theta_r}^2 + Y_{\theta_r}^2}$$
$$\rho_{\beta_r} = \sqrt{X_{\beta_r}^2 + Y_{\beta_r}^2} \tag{18}$$

denote the lengths of the mean vectors. They are used in the definition of the dispersion of the angles by means of their angular deviation according to [48]:

$$s(\theta_r) = \sqrt{2(1-\rho_{\theta_r})} \quad [\text{rad}]$$
$$s(\beta_r) = \sqrt{2(1-\rho_{\beta_r})} \quad [\text{rad}] \tag{19}$$

Fig. 8 shows the statistical consolidation of ACDM data for a measuring stage close to the ultimate load of the large-scale homogeneous element test SL-1 [11]. Reliable raw ACDM data are indicated in black and data that includes imputed crack kinematics in magenta. Fig. 8 (a) shows the crack pattern with corresponding crack widths. Similarly to the test PT-1(see Section 2.3.5), a significant fraction of the crack kinematics had to be imputed due to the highly complex crack pattern with a high amount of unreliable measurements. In Fig. 8(b), the weighted mean crack inclination $\bar{\theta}_r$ and the crack kinematic vector direction $\bar{\beta}_r$ including their angular deviations $s(\theta_r)$ and $s(\beta_r)$ are shown. In addition, the relative crack area density estimations of θ_r and β_r are shown for comparison. The relative crack area a_r is defined as the ratio between the total crack area $\sum_{i=1}^{n} \|\boldsymbol{\delta}_i\| l_i$ and the corresponding examined concrete surface in the undeformed state A_c:

$$a_r = \frac{\sum_{i=1}^{n} \|\boldsymbol{\delta}_i\| l_i}{A_c} \tag{20}$$

The relative crack area density estimations are obtained by means of kernel density estimations, where the kernel of each crack point is scaled with its incremental crack area according to Eq. (20). In their computation, a circular normal (von Mises) kernel [49] is applied, where it is again accounted for the bidirectionality of the crack inclinations θ_r. While in Fig. 8(b) the weighted crack inclinations θ_r approximately follow a (circular) normal distribution, the crack kinematic vector directions β_r exhibit two peaks at approximately 64° and 71° and a minor peak at 90°. These peaks are more pronounced in the data with imputed crack kinematics. The first two peaks indicate two slightly different dominant crack opening directions. The third minor peak at 90° can be explained by cracks aligning with the horizontal (stronger) reinforcing bars. Nevertheless, the mean angles $\bar{\theta}_r$ and $\bar{\beta}_r$ contain valuable information. Their relevance in representing the actual crack behaviour is discussed in Section 3.4.

The relative crack area density estimation of δ is shown in Fig. 8(c). The density functions and histograms are obtained analogously to those for the angles θ_r and β_r, but with a Gaussian kernel (restricted to positive values). Although the most significant part of the crack area is explained by cracks with a width of about 1.25 mm, and an average crack opening could be determined, the relevance of such values for the mechanical behaviour is questionable: Especially for complex patterns, mean values of crack widths lack representativeness. In the present approach, an upper quantile is proposed instead (see Section 3.4).

By comparing the results from the raw crack kinematic measurements (with removed unreliable data) to the data that includes imputed crack kinematics, it is shown that the distributions are approximately affine and that the mean angles differ by less than 1°(Fig. 8). This indicates that the unreliable measurements are fairly evenly distributed with respect to θ_r and β_r. The relative crack area of the (reliable) raw data and the data with imputed crack kinematics results in 0.56% and 0.95%, respectively, implying that only about 60% of the crack area can be measured directly without the need for data imputation in this case. In Section 3.4, it is shown that ACDM with data imputation reliably captures the complete crack area.

3.3. Best-fit homogeneous strain and cracks

3.3.1. Overview

In contrast to the approach to extract crack characteristics presented in Section 3.2, consisting of the statistical consolidation of the results obtained with the refined ACDM, the second approach, outlined below, directly uses the full-field DIC displacement measurements. Here, the characteristic crack width, slip, inclination and spacing of a homogeneous element are determined with their best-fit values. As typically assumed by established and widely used mechanical models for reinforced concrete (e.g. [4–6]), a homogeneous crack pattern with one set of straight parallel cracks with uniform spacing, opening direction and opening magnitude is assumed. The approach consists of seeking the crack characteristics that best fit the full-field DIC displacement measurement, given this assumption. For that purpose, the best-fit homogeneous strain is required in the first step. The resulting residuals in its computation are then used to extract the best-fit homogeneous crack

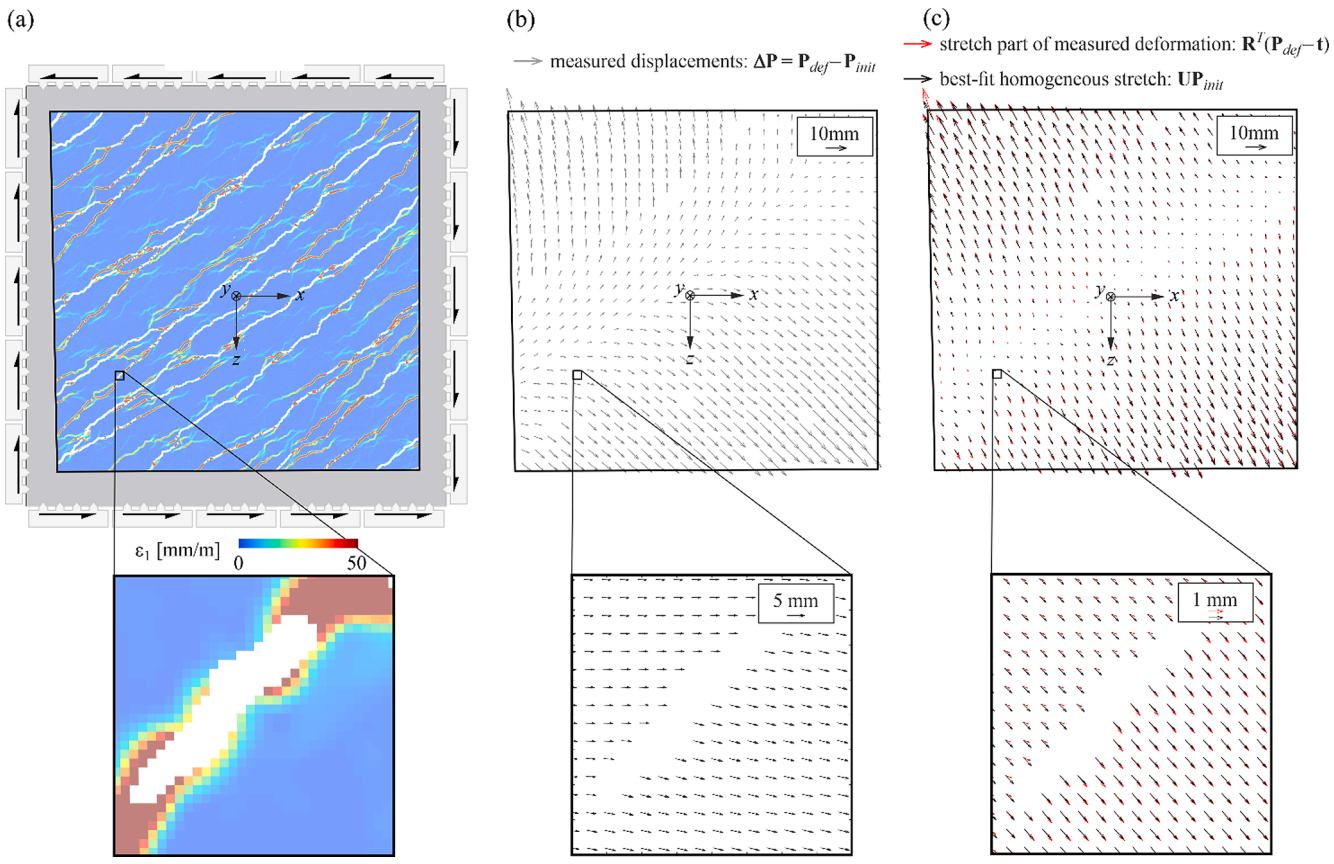

Fig. 9. Best-fit homogeneous deformation of SL-1 at ultimate load with 1.7 × 10^6 DIC measuring points: (a) major principal strain magnitudes; (b) measured displacements of the specimen; (c) stretch part of the measured deformation by removing the best-fit rotation **R** and translation **t**, and best-fit homogeneous stretch $\mathbf{UP}_{init}$. In (c) and (b), a step of 50 (and in the zoomed-in windows a step of 2) are used to visualise the displacements and deformations.

characteristics. The procedure is again illustrated using DIC measurements obtained from VIC-3D [42].

3.3.2. Best-fit homogeneous strain

In the Lagrangian description – where the deformed position of a point is described in terms of its initial position and a displacement vector – the homogeneous in-plane deformation of a 2D point is:

$$\mathbf{p}_{def,hom} = \mathbf{F}\mathbf{p}_{init} + \mathbf{t} \tag{21}$$

In Eq. (21), $\mathbf{p}_{init}$ is the undeformed (initial) position of a point, $\mathbf{p}_{def,hom}$ its homogeneously deformed position, **F** the deformation gradient tensor and **t** a translation:

$$\mathbf{p}_{init} = \begin{bmatrix} x_{init} \\ z_{init} \end{bmatrix}, \quad \mathbf{p}_{def,hom} = \begin{bmatrix} x_{def,hom} \\ z_{def,hom} \end{bmatrix}$$
$$\mathbf{F} = \begin{bmatrix} f_{xx} & f_{xz} \\ f_{zx} & f_{zz} \end{bmatrix}, \quad \mathbf{t} = \begin{bmatrix} t_x \\ t_z \end{bmatrix} \tag{22}$$

For a homogeneous in-plane deformation, **F** and **t** are both uniform, i.e. independent of the coordinates and thus constant. In general, **F** is a non-symmetric tensor. It can be decomposed into a symmetric stretch tensor and a pure rotation, as further outlined below. Estimating the best-fit in-plane homogeneous deformation from full-field DIC measurements of a specimen's surface is a least-square problem. It consists of finding the values of **F** and **t** minimising the sum of squared differences between the measured (i.e. $\mathbf{p}_{init,i} + \mathbf{\Delta p}_i$) and estimated homogeneous deformed positions (i.e. $\mathbf{F}\mathbf{p}_{init,i} + \mathbf{t}$) of all k DIC measuring points, i.e.:

$$(\mathbf{F}, \mathbf{t}) = \underset{\mathbf{F}\in\mathbb{R}^{2\times2},\mathbf{t}\in\mathbb{R}^2}{\operatorname{argmin}} \sum_{i=1}^{k} w_i \left\| \left(\mathbf{F}\mathbf{p}_{init,i} + \mathbf{t}\right) - \left(\mathbf{p}_{init,i} + \mathbf{\Delta p}_i\right) \right\|^2 \tag{23}$$

where $\mathbf{p}_{init,i}$ is the undeformed position of measuring point i and $\mathbf{\Delta p}_i$ its displacement. In Eq. (23), each measuring point is weighted to account for its uncertainty. The weights are set to $w_i = 1/\sigma^2_{DIC,i}$ where $\sigma_{DIC,i}$ is the confidence interval for the match at this point in pixels, computed directly in VIC-3D [42]. The solving procedure of Eq. (23) is shown in Appendix B.

As mentioned, the best-fit deformation gradient tensor **F** computed in Eq. (23) can be decomposed into a symmetric stretch tensor **U** or **V** and a rotation **R**. This separation of **F** is known as polar decomposition:

$$\mathbf{F} = \mathbf{RU} = \mathbf{VR} \tag{24}$$

In Eq. (24), **RU** denotes the right polar decomposition, where the element is stretched first and then rotated, and **VR** the left polar decomposition with reversed order of the two operations (see Fig. 10 (d)). The polar decomposition can be obtained by using the singular value decomposition (SVD) of **F**:

$$\mathbf{F} = \mathbf{W\Sigma Q}^T \tag{25}$$

Where **W** and **Q** are orthonormal 2 × 2 matrices and **Σ** is a 2 × 2 diagonal matrix with non-negative diagonal elements. The rotation matrix **R** (that rotates the element through the angle ω) is then:

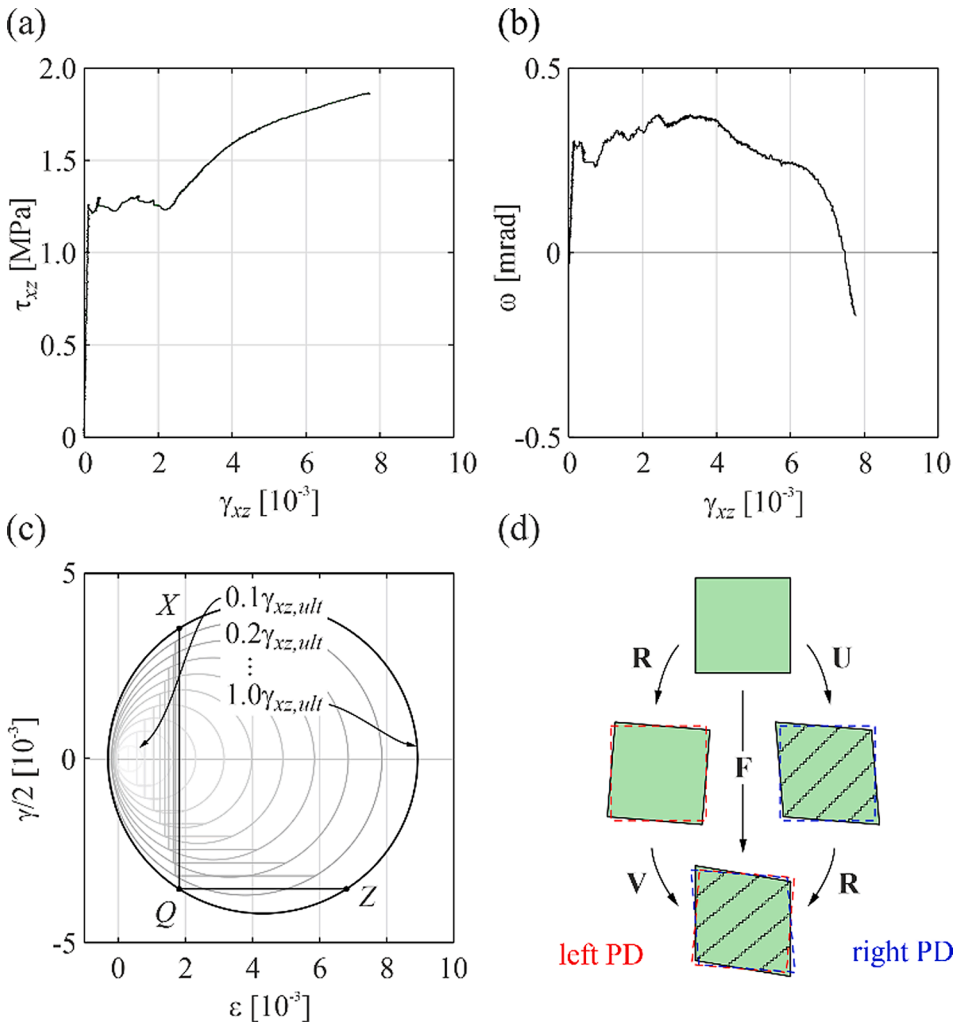

Fig. 10. Best-fit homogeneous strain of SL-1: (a) load-deformation behaviour (best-fit shear strain γ_{xz} versus shear stress τ_{xz}); (b) rotation of the specimen; (c) Mohr circles of best-fit strains at selected measuring stages; (d) left and right polar decomposition of deformation gradient tensor **F**.

$$\mathbf{R} = \mathbf{W}\mathbf{Q}^T = \begin{bmatrix} \cos(\omega) & -\sin(\omega) \\ \sin(\omega) & \cos(\omega) \end{bmatrix} \tag{26}$$

and the right and left stretch tensors are:

$$\mathbf{U} = \mathbf{R}^{\mathbf{T}}\mathbf{F}, \quad \mathbf{V} = \mathbf{F}\mathbf{R}^{\mathbf{T}} \tag{27}$$

In Fig. 9, the best-fit homogeneous deformation of SL-1 at the measuring stage close to the failure is shown. Fig. 9(a) indicates the major principal strain field of this measuring stage with colours. Fig. 9 (b) shows the measured displacements $\mathbf{\Delta P} = \mathbf{P}_{def} - \mathbf{P}_{init}$ (with $\mathbf{P}_{init} = \left[\mathbf{p}_{init,1}, \ldots, \mathbf{p}_{init,k}\right]$ and $\mathbf{P}_{def} = \left[\mathbf{p}_{def,1}, \ldots, \mathbf{p}_{def,k}\right]$). The stretch part of the best-fit homogeneous deformation using the more common right polar decomposition ($\mathbf{UP}_{init}$) is shown in Fig. 9(c). Additionally, the stretch part of the measured deformation ($\mathbf{R}^T(\mathbf{P}_{def} - \mathbf{t})$) is shown.

In the following, the transformation of the deformation gradient tensor **F** into the engineering strain notation, commonly used in mechanics of structural concrete, is shown. To this end, the right Lagrangian strain tensor **E** is computed first:

$$\mathbf{E} = \begin{bmatrix} e_{xx} & e_{xz} \\ e_{zx} & e_{zz} \end{bmatrix} = \frac{1}{2}\left(\mathbf{U}^2 - \mathbf{I}\right) = \frac{1}{2}\left(\mathbf{F}^T\mathbf{F} - \mathbf{I}\right) \tag{28}$$

whose elements are used to describe the engineering normal and shear strains (i.e., change of physical lengths and angles with respect to the initial configuration) as follows:

$$\boldsymbol{\varepsilon} = \begin{bmatrix} \varepsilon_{xx} & \gamma_{xz}/2 \\ \gamma_{zx}/2 & \varepsilon_{zz} \end{bmatrix} = \begin{bmatrix} \sqrt{1+2e_{xx}} - 1 & \sin^{-1}\left(2e_{xz}\Big/\sqrt{(1+2e_{xx})(1+2e_{zz})}\right) \\ \sin^{-1}\left(2e_{xz}\Big/\sqrt{(1+2e_{xx})(1+2e_{zz})}\right) & \sqrt{1+2e_{zz}} - 1 \end{bmatrix} \tag{29}$$

In Fig. 10, the load-deformation behaviour of SL-1 is shown with the shear stresses τ_{xz} plotted against the shear strains γ_{zx} in Fig. 10(a). For comparison, the shear strains were also computed using the less

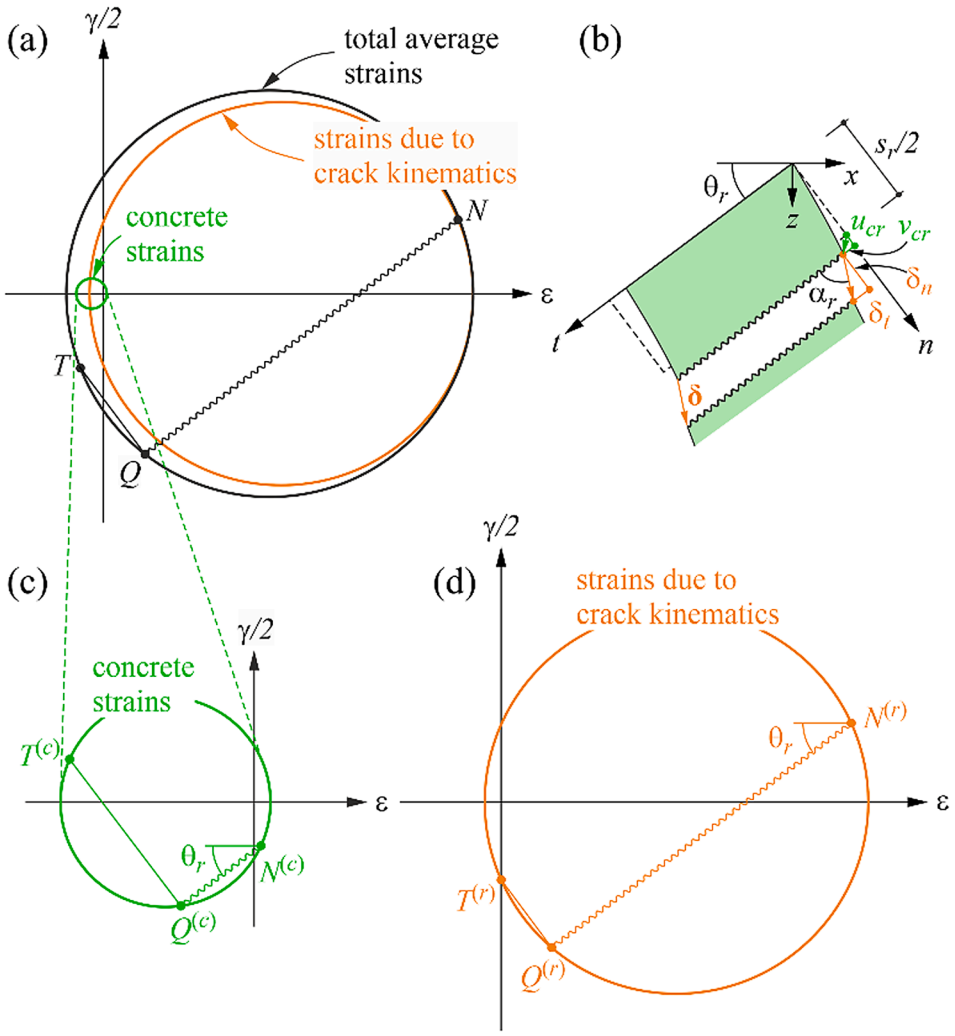

Fig. 11. Strain compatibility (adopted from [51]): (a) decomposition of measured total strains into concrete strains and strains due to crack kinematics; (b) notation of displacements and crack kinematics; (c) concrete strains; (d) strains due to crack kinematics.

common left polar decomposition (see Fig. 10(d) and thus, $\mathbf{U}$ and $\mathbf{F}^T\mathbf{F}$ in Eq. (28) are replaced with $\mathbf{V}$ and $\mathbf{F}\mathbf{F}^T$, respectively), however leading only to marginal differences (less than 2 μm/m throughout the test). This is explained by the fact that the specimen rotation is very small, as shown in Fig. 10(b). The evolution of the specimen's best-fit homogeneous deformation is shown in Fig. 10(c) by means of Mohr circles of strains.

3.3.3. *Best-fit homogeneous crack characteristics*

The obtained homogeneous strains of an element test are used in combination with the residuals in their computation to extract the best-fit set of straight parallel cracks with uniform spacing, opening direction and opening magnitude, which are referred to as homogeneous crack characteristics in the following. For this purpose, in a first step, the best-fit total strains $\boldsymbol{\varepsilon}$ are subdivided into strains due to the deformations of the concrete between the cracks $\boldsymbol{\varepsilon}^{(c)}$ and strains caused by crack kinematics $\boldsymbol{\varepsilon}^{(r)}$ ($\boldsymbol{\varepsilon} = \boldsymbol{\varepsilon}^{(c)} + \boldsymbol{\varepsilon}^{(r)}$), see Fig. 11. This approach has been proposed by [50] and is consistently used e.g. in [4,51]. It is mentioned that the strains $\boldsymbol{\varepsilon}$, $\boldsymbol{\varepsilon}^{(c)}$ and $\boldsymbol{\varepsilon}^{(r)}$ denote constant average values over a crack element. Hence, for any crack inclination θ_r and crack kinematic vector direction β_r the strains due to crack kinematics $\boldsymbol{\varepsilon}^{(r)}$ are:

$$\varepsilon_n^{(r)} = \frac{\delta_n}{s_r}, \quad \varepsilon_t^{(r)} = 0, \quad \gamma_{nt}^{(r)} = \frac{\delta_t}{s_r} \tag{30}$$

where the *n*-direction coincides with θ_r and the *t*-direction is perpendicular to it.

Since only measurements of total strains are available, the decomposition into $\boldsymbol{\varepsilon}^{(c)}$ and $\boldsymbol{\varepsilon}^{(r)}$ requires further simplifications (i.e. assuming a reasonable value for the crack inclination). For the typical case with $\varepsilon_3 \leqslant 0$, it is assumed that the principal direction of concrete compressive strains coincides with θ_r and the concrete between cracks exhibits no strains perpendicular to θ_r ($\varepsilon_1^{(c)} = 0$), which also implies that $\varepsilon_1^{(r)} = \varepsilon_1$. Hence, the negative strains are caused by either the crack kinematics or concrete compression. These are reasonable assumptions, having a minor effect on the results since $\varepsilon_1^{(c)} \ll \varepsilon_1^{(r)}$ due to the low tensile concrete strength. As a consequence, all possible solutions for the strain decomposition range between the situations shown in Fig. 12(c) and (e). These two boundary cases denote situations with vanishing concrete deformation ($\boldsymbol{\varepsilon}^{(c)} = \mathbf{0}$). The special case of orthogonally opening cracks ($\delta_t = 0$) and thus $\varepsilon_3^{(c)} = \varepsilon_3$ is shown in Fig. 12(d). This decomposition also illustrates the sign change of δ_t, when successively varying from the situation in Fig. 12(c) to Fig. 12(e). However, in most applications, the sign of δ_t can be predetermined based on the experimental configuration

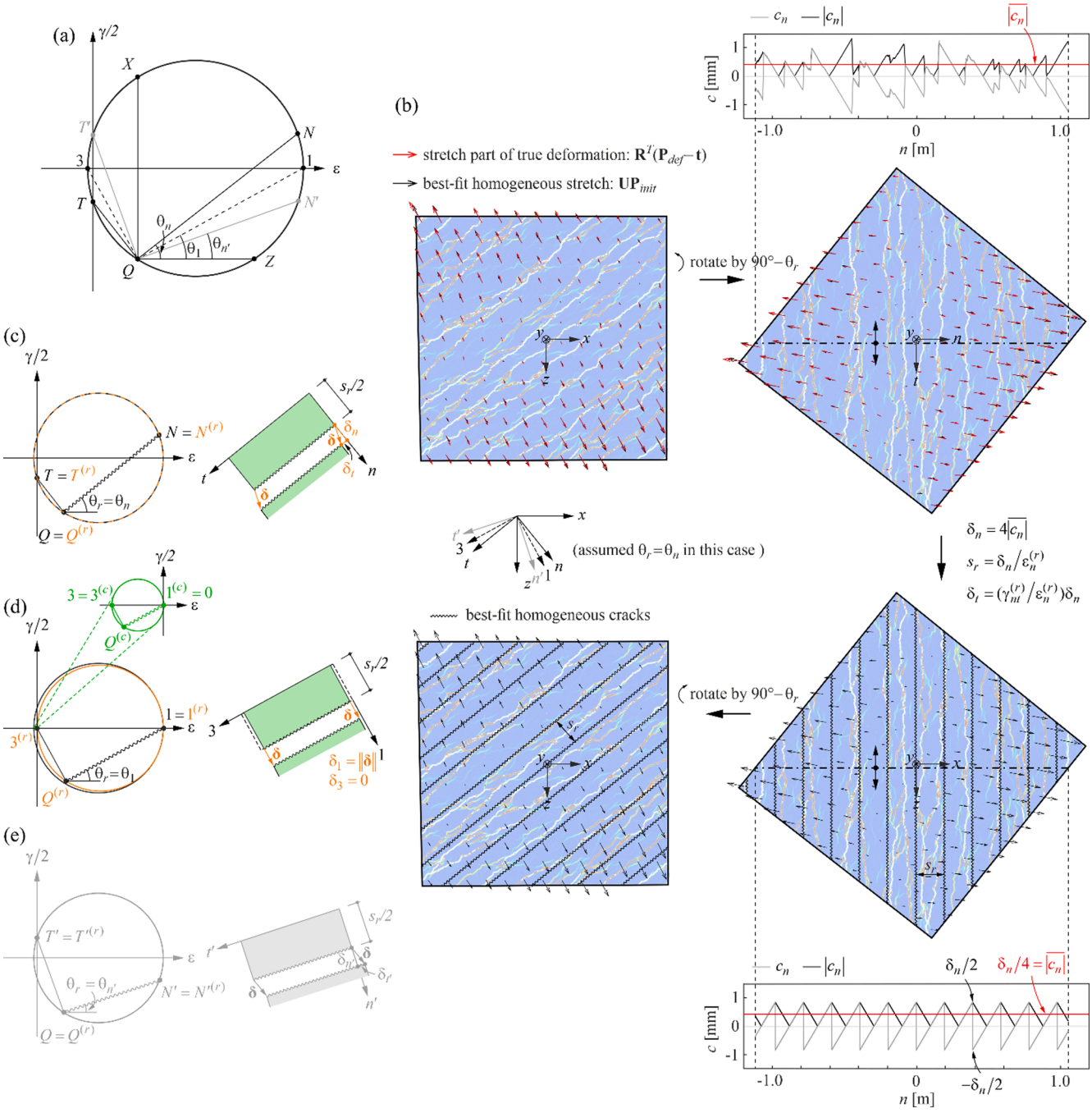

Fig. 12. Best-fit homogenous crack characteristics for SL-1 at ultimate load: (a) range of possible solutions for the strain decomposition of measured total strains and the resulting crack inclination θ_r; (b) details of the best-fit homogenous crack opening extraction (perpendicular to θ_r) assuming $\theta_r = \theta_n$; (c) –(e) strain decompositions with corresponding concrete deformations and crack kinematics for $\theta_r = \theta_n$, $\theta_r = \theta_1$, $\theta_r = \theta_{n'}$, respectively.

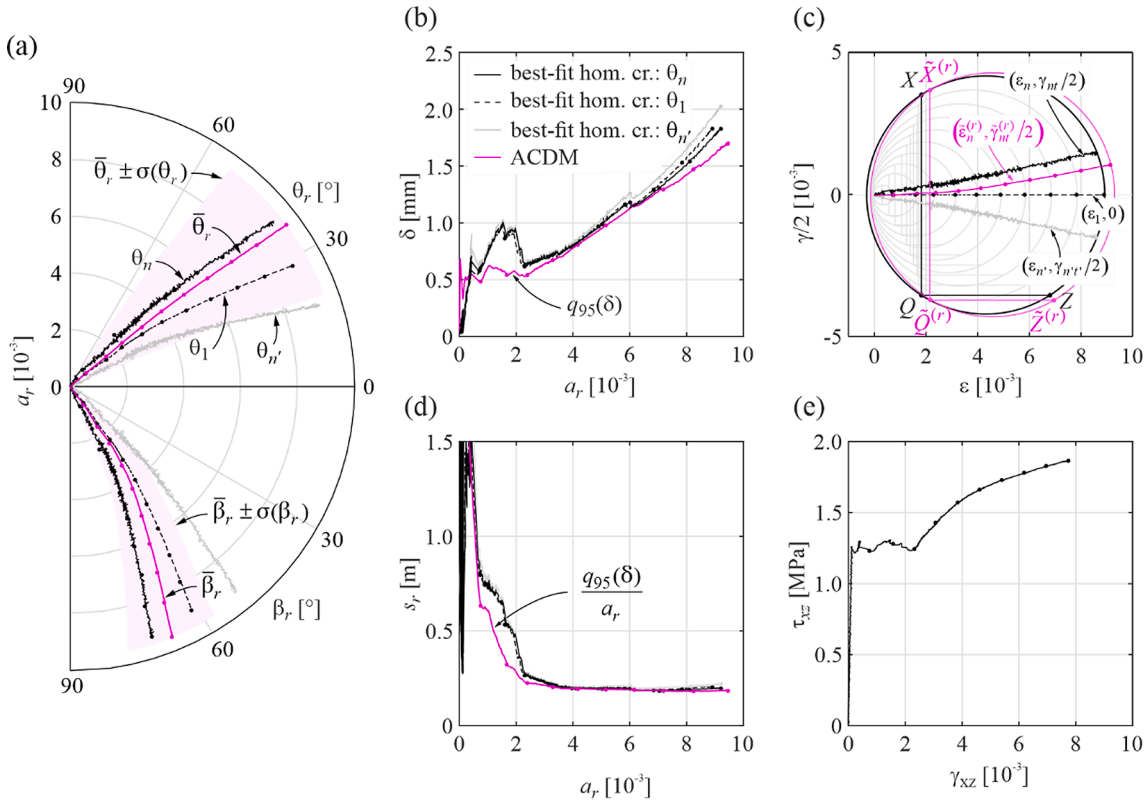

Fig. 13. Comparison of homogeneous crack characteristics extracted from ACDM data (Section 3.2) and the best-fit approach (Section 3.3): (a) characteristic crack inclination θ_r and crack kinematic vector direction β_r versus relative crack area a_r; (b) relative crack area a_r versus characteristic crack kinematic vector magnitude δ; (c) Mohr circles of strain at selected measuring stages; (d) relative crack area a_r versus characteristic crack spacing s_r; (e) load-deformation behaviour (best-fit shear strain γ_{xz} versus shear stress τ_{xz}).

and thus, the range of plausible solutions is reduced by half. In SL-1, which is loaded in pure shear and where the vertical reinforcement is significantly weaker than the horizontal one, positive δ_t are expected (and thus, $\theta_r \in [\theta_1, \theta_n]$). Therefore, only strain decompositions between Fig. 12(c) and (d) are considered as plausible solutions. Nevertheless, in Fig. 12(a), the range of all theoretically possible crack inclinations $\theta_r \in [\theta_{n'}, \theta_n]$ is shown. It should be noted that for the case $\varepsilon_3 > 0$ (which may generally occur, e.g. due to lateral concrete expansion under compression or multiple cracks with different inclinations), neglecting concrete tensile strains cannot lead to any consistent solution for the strain decomposition. For such cases, $\varepsilon_3^{(c)} = 0$ and $\varepsilon_1^{(c)} = \varepsilon_3$ are assumed instead, leading to $\varepsilon_3^{(r)} = 0$ and $\varepsilon_1^{(r)} = \varepsilon_1 - \varepsilon_3$. In the pure shear test SL-1, strain states with $\varepsilon_3 > 0$ only occurred in the very early cracking stage of the experiment, for $\gamma_{xz} < 0.4‰$.

Once a certain crack inclination in the discussed theoretical range has been assumed, the remaining homogeneous crack characteristics, δ_n, δ_t and s_r, are solved by analysing the residuals obtained in the computation of the best-fit homogeneous strain. The rotation-independent part of the measured deformation, i.e. the stretch $\mathbf{R}^T(\mathbf{P}_{def} - \mathbf{t})$, is compared to the best-fit homogeneous stretch $\mathbf{UP}_{init}$ (see Fig. 12(b)). Thus, for each measuring point i, the (rotation-independent) residual is:

$$\mathbf{c}_i = \mathbf{Up}_{init,i} - \mathbf{R}^T(\mathbf{P}_{def} - \mathbf{t}) \tag{31}$$

In Fig. 12(b), the steps for extracting the characteristic crack kinematics and spacing that correspond to $\theta_r = \theta_n$ are shown; the solutions for all possible situations that correspond to $\theta_{n'} \leqslant \theta_r \leqslant \theta_n$ can be obtained analogously. The characteristic homogeneous crack opening is determined based on the residual component perpendicular to the crack inclination θ_r, noting that these residual components reflect the discontinuous variation of the rotation-independent part of the deformations caused by crack opening. Under the assumption of homogeneous crack characteristics (in combination with the assumed negligible concrete strains perpendicular to the crack inclination), a relationship between the residuals and the crack opening (Fig. 12(b)) exists, i.e.:

$$\delta_n = 4|\overline{c_n}| \tag{32}$$

This relationship is applied to the measured residuals in Eq. (31) (see Fig. 12(b)). Finally, the best-fit homogeneous crack spacing and sliding are obtained by using Eqs. (30) and (32) as follows:

$$s_r = \frac{\delta_n}{\varepsilon_n^{(r)}} \tag{33}$$

$$\delta_t = \gamma_{nt}^{(r)} s_r = \frac{\gamma_{nt}^{(r)}}{\varepsilon_n^{(r)}} \delta_n \tag{34}$$

3.4. Discussion

In Fig. 13, both approaches for the extraction of homogeneous crack characteristics proposed in Sections 3.2 and 3.3 are compared. For this purpose, the evaluation of crack inclinations, spacing and crack kinematics are analysed for SL-1. In this section, the results of ACDM data that includes imputed crack kinematics are used, as they provide an estimation of the complete data.

The comparison of relative crack areas and strains in the two different approaches requires the following conversions. In the best-fit homogeneous crack characteristics approach (Section 3.3), the relative crack area $\widehat{a}_r$ uses the definition in Eq. (20) and simplifies to:

$$\widehat{a}_r = \frac{\delta}{s_r} = \frac{\sqrt{\delta_n^2 + \delta_t^2}}{s_r} = \sqrt{\left(\varepsilon_n^{(r)}\right)^2 + \left(\gamma_{nt}^{(r)}\right)^2} \tag{35}$$

On the other hand, the induced strains due to crack kinematics obtained from the statistical consolidation of ACDM data $\widetilde{\boldsymbol{\varepsilon}}^{(r)}$ (shown in Fig. 13(c)) results in:

$$\begin{aligned}\widetilde{\varepsilon}_n^{(r)} &= \frac{\delta_n}{s_r} = \frac{\sin\left(\overline{\alpha}_r\right)\delta}{s_r} = \sin\left(\overline{\alpha}_r\right)a_r \\ \widetilde{\varepsilon}_t^{(r)} &= 0 \\ \widetilde{\gamma}_{nt}^{(r)} &= \frac{\delta_t}{s_r} = \frac{\cos\left(\overline{\alpha}_r\right)\delta}{s_r} = \cos\left(\overline{\alpha}_r\right)a_r\end{aligned} \tag{36}$$

where $\overline{\alpha}_r = 180^\circ - \overline{\theta}_r - \overline{\beta}_r$ (see the definition of α_r in Fig. 2(f)). It is important to note that the strain $\widetilde{\boldsymbol{\varepsilon}}^{(r)}$ is fully determined by the relative crack area and the mean crack opening angle $\overline{\alpha}_r$, and no statistical values for crack kinematics and crack spacings from ACDM data is required. In Eqs. (35) and (36), the circumflex and tilde diacritics are used to distinguish the two approaches.

In Fig. 13(a) and (c), it is shown that the mean crack inclination $\overline{\theta}_r$ and the crack kinematic vector direction $\overline{\beta}_r$ obtained from ACDM are in the range of plausible results predicted in Section 3.3 ($\theta_r \in [\theta_1, \theta_n]$ and the corresponding range of realistic angles β_r). At the beginning of the test, the results from ACDM data align well with the best-fit homogeneous crack characteristics obtained for θ_1, whereas in later load stages, a shift towards the solution for θ_n is observed. This behaviour can be explained by the strains due to crack kinematics $\boldsymbol{\varepsilon}^{(r)}$ that increasingly dominate the strains due to the deformations of the concrete between the cracks $\boldsymbol{\varepsilon}^{(c)}$ during the test. However, note that the data obtained with ACDM show a relatively high scatter (see magenta areas in Fig. 13(a)).

Furthermore, it is shown that the refined ACDM captures the crack area very accurately. The relative crack area α_r obtained by the refined ACDM only slightly overestimates the results of the best-fit homogeneous strain in Fig. 13(c). Note here that almost 40% of the crack area in the refined ACDM is obtained from imputed and not directly measured crack kinematics (see Section 3.2).

In Fig. 13(b) and (d), the best-fit homogeneous crack kinematic vector length δ and crack spacing s_r are both more or less independent of the assumed crack inclination θ_r. Similar results are obtained with ACDM when referring to the 95%-quantile of δ. With this quantile, significant differences are only observed in the crack formation phase (for $\gamma_{xz} < 2‰$, see also Fig. 13(e)), where large crack spacings are estimated, and thus, the assumption of a homogeneous crack pattern in the experiment is inappropriate. To assess the possible validity of the 95%-quantile of δ from ACDM data in characterising the crack behaviour in homogeneous large-scale element tests, evaluations of further experiments will be necessary.

4. Concluding remarks

This publication proposes essential refinements in the automatic detection of cracks and extraction of crack kinematics from full-field digital image correlation (DIC) measurements, which allow reliably assessing the crack behaviour even in large-scale experiments of (quasi-) brittle material with complex crack patterns. The refinements apply to the original automatic crack detection and measurement (ACDM) procedure [10] proposed by the authors of this paper, which is implemented in an open-source software with a graphical user interface. The two major refinements involve:(i) a direction-independent Canny edge-based crack detector that refers to the major principal tensile strain field and extracts cracks as traceable skeletons at high strain magnitudes, and (ii) a consistent and accurate procedure to measure local crack kinematics that includes the assessment of the measurement reliability. The refined ACDM procedure has been applied to large-scale shear panel experiments of a size of 2.0 × 2.0 m with highly complex crack patterns. Compared to the original ACDM,(i) much finer cracks have been detected (up to cracks width of 0.02 px, which is four times thinner than the minimum detectable crack reported in [10]), (ii) crack locations are detected much more accurately, especially at crack intersections, (iii) the setup of reference points used to describe the crack face displacements is automatically optimised based on the local conditions, leading to much higher reliabilities of the crack kinematic measurements, and (iv) unreliable crack kinematic measurements are automatically identified, removed and substituted with their best possible estimation based on reliable neighbouring data.

These refinements are required to obtain accurate and reliable measurements of the crack behaviour, which is crucial, especially in the statistical consolidation of the detailed data into more understandable characteristic values. For the case of homogeneous experiments (in terms of loading, boundary conditions, geometry, material and reinforcement), which are highly relevant for understanding the mechanical behaviour of the tested material and in the model verification, the extraction of characteristic values from the ACDM data is proposed. For that purpose, one set of straight parallel cracks with uniform spacing, opening direction and magnitude is assumed, which is in accordance with established and widely used mechanical models. The crack behaviour can be characterised by referring to the mean crack inclination and crack kinematic vector direction (weighted by the local crack area associated with the crack measuring point) and to a certain quantile of the crack kinematic magnitudes.

The characteristic crack properties in homogeneous experiments obtained from ACDM data are compared to a more straightforward approach consisting of the estimation of the best-fit homogeneous crack characteristics by directly referring to the full-field DIC displacements. Here, the best-fit homogeneous strains are computed in a least-square sense first and then converted to the best-fit crack kinematics, crack inclination and crack spacing by analysing the residuals. This approach is not unique and provides a range of possible solutions. However, if simple and reasonable assumptions are made about the deformation of the uncracked concrete between cracks, the range of realistic solutions can be strongly narrowed and the best-fit crack kinematics and crack spacing become almost unique. The results of the statistical consolidation of ACDM data are very similar to the ones provided by the best-fit approach when choosing a 95%-quantile of the ACDM crack kinematic quantities and generally. This simpler approach is computationally less demanding and hence faster, and generally in good agreement with the global crack behaviour for homogeneous experiments. However, ACDM is a much more powerful tool as it (i) provides much more detailed insights on the mechanical behaviour of structural experiments by detecting exact positions of cracks and measuring quasi-continuous crack kinematics along cracks, and (ii) is also applicable to non-homogeneous experiments.

CRediT authorship contribution statement

Nicola Gehri: Conceptualization, Methodology, Project administration, Software, Validation, Visualization, Writing – original draft. **Jaime Mata-Falcón:** Conceptualization, Supervision, Writing – review & editing. **Walter Kaufmann:** Conceptualization, Writing – review & editing.

Declaration of Competing Interest

The authors declare that they have no known competing financial interests or personal relationships that could have appeared to influence the work reported in this paper.

Appendix A

This appendix presents the solution procedure of Eq. (2) for the best-fit in-plane rigid body motion of the reference points that define the crack face displacements as proposed in Section 2.3.2. For the sake of simplicity, only the solution procedure for crack side A is given here. Note that the same applies to crack side B by replacing the corresponding variables and indices in the formulas.

For the set of m reference points at side A of crack point i, the best-fit rotation $\mathbf{R}_{Ai}$ and translation $\mathbf{t}_{Ai}$ are sought. Eq. (2) is restated hereafter:

$$(\mathbf{R}_{Ai}, \mathbf{t}_{Ai}) = \underset{\mathbf{R}_{Ai}\in SO(2), \mathbf{t}_{Ai}\in\mathbb{R}^2}{\operatorname{argmin}} \sum_{j=1}^{m} w_{Aij} \left\| \left(\mathbf{R}_{Ai}\mathbf{a}_{ij} + \mathbf{t}_{Ai}\right) - \left(\mathbf{a}_{ij} + \boldsymbol{\delta}_{Aij}\right) \right\|^2 \tag{A.1}$$

where $\mathbf{a}_{ij}$ denotes the in-plane positions of the reference points in the undeformed state, $\boldsymbol{\delta}_{Aij}$ the corresponding displacement vectors and w_{Aij} the weights of the reference points. The solution of Eq. (A.1) is obtained with a method proposed by Sorkine-Hornung and Rabinovich [44]. The computation steps are summarised in the following:

1. Compute the weighted centroids of the set of reference points in the undeformed (initial) and deformed state:

$$\bar{\mathbf{a}}_{init,i} = \frac{\sum_{j=1}^{m} w_{Aij}\mathbf{a}_{ij}}{\sum_{j=1}^{m} w_{Aij}}, \quad \bar{\mathbf{a}}_{def,i} = \frac{\sum_{j=1}^{m} w_{Aij}\left(\mathbf{a}_{ij} + \boldsymbol{\delta}_{Aij}\right)}{\sum_{j=1}^{m} w_{Aij}} \tag{A.2}$$

2. Compute the position of the reference points in the undeformed and deformed state with respect to the centroids:

$$\widehat{\mathbf{a}}_{init,ij} = \mathbf{a}_{ij} - \bar{\mathbf{a}}_{init,i}, \quad \widehat{\mathbf{a}}_{def,ij} = \mathbf{a}_{ij} + \boldsymbol{\delta}_{Aij} - \bar{\mathbf{a}}_{def,i}, \quad j = 1, 2, \ldots, m \tag{A.3}$$

3. By using the definitions in Eq. (A.3), reformulate the problem in Eq. (A.1) independent of $\mathbf{t}_{Ai}$:

$$\mathbf{R}_{Ai} = \underset{\mathbf{R}_{Ai}\in SO(2)}{\operatorname{argmin}} \sum_{j=1}^{m} w_{Aij} \left\| \mathbf{R}_{Ai}\widehat{\mathbf{a}}_{init,ij} - \widehat{\mathbf{a}}_{def,ij} \right\|^2 \tag{A.4}$$

(A.4) is known as the orthogonal Procrustes rotation problem [52,53]. The solving procedure for finding the optimum rotation $\mathbf{R}_{Ai}$ includes the following steps (4–7).

4. Compute the 2×2 covariance matrix:

$$\mathbf{S}_i = \widehat{\mathbf{A}}_{init,i}\mathbf{W}_i\widehat{\mathbf{A}}_{def,i}^T \tag{A.5}$$

where $\widehat{\mathbf{A}}_{init,i} = \left[\widehat{\mathbf{a}}_{init,i1}, \ldots, \widehat{\mathbf{a}}_{init,im}\right]$ and $\widehat{\mathbf{A}}_{def,i} = \left[\widehat{\mathbf{a}}_{def,i1}, \ldots, \widehat{\mathbf{a}}_{def,im}\right]$ are matrices containing the centred positions of the reference points in the undeformed and deformed state as their columns, respectively, and $\mathbf{W}_i = \operatorname{diag}(w_{i1}, \ldots, w_{im})$ is a $m \times m$ diagonal matrix with weights w_{ij} on diagonal entry j.

5. Compute the singular value decomposition of the covariance matrix:

$$\mathbf{S}_i = \mathbf{U}_i\boldsymbol{\Sigma}_i\mathbf{V}_i^T \tag{A.6}$$

6. Compute the best-fit 2D rigid rotation of the crack face:

$$\mathbf{R}_{Ai} = \mathbf{V}_i \begin{pmatrix} 1 & 0 \\ 0 & \det\left(\mathbf{V}_i\mathbf{U}_i^T\right) \end{pmatrix} \mathbf{U}_i^T \tag{A.7}$$

Note that the term $\det(\mathbf{V}_i\mathbf{U}_i^T)$ in Eq. (A.7) is used to constrain the solution to rotations (with $\det(\mathbf{R}_{Ai}) = 1$). Computing $\mathbf{R}_{Ai} = \mathbf{V}_i\mathbf{U}_i^T$ leads to an orthonormal matrix, which, however, could also include non-realistic reflections. The restriction of the solution to rotations is essential here because the reference points lie more or less on a line, and therefore, the fit would be prone to include reflections.

7. Compute the best-fit rigid translation:

$$\mathbf{t}_{Ai} = \bar{\mathbf{a}}_{def,i} - \mathbf{R}_{Ai}\bar{\mathbf{a}}_{init,i} \tag{A.8}$$

Appendix B

This appendix presents the solution procedure of Eq. (23) for the best-fit in-plane homogeneous deformation from full-field DIC displacement measurements.

For a set of k measuring points of in-plane displacements, the best-fit deformation gradient tensor $\mathbf{F}$ and translation $\mathbf{t}$ is sought. Eq. (23) is restated

hereafter:

$$(\mathbf{F},\mathbf{t}) = \underset{\mathbf{F}\in\mathbb{R}^{2\times2},\mathbf{t}\in\mathbb{R}^2}{\operatorname{argmin}} \sum_{i=1}^{k} w_i \left\| \left(\mathbf{F}\mathbf{p}_{init,i} + \mathbf{t}\right) - \left(\mathbf{p}_{init,i} + \mathbf{\Delta p}_i\right) \right\|^2 \tag{B.1}$$

where $\mathbf{p}_{init,i}$ denotes the in-plane positions of the measuring points in the undeformed state and $\mathbf{\Delta p}_i$ the corresponding displacement vectors. w_{Aij} are the weights of the measuring points. The steps for solving Eq. (B.1) are summarised in the following:

1. Compute the weighted centroids of the set of measuring points in the undeformed (initial) and deformed state:

$$\overline{\mathbf{p}}_{init} = \frac{\sum_{i=1}^{k} w_i \mathbf{p}_{init,i}}{\sum_{i=1}^{k} w_i}, \quad \overline{\mathbf{p}}_{def} = \frac{\sum_{i=1}^{k} w_i \left(\mathbf{p}_{init,i} + \mathbf{\Delta p}_i\right)}{\sum_{i=1}^{k} w_i} \tag{B.2}$$

2. Compute the position of the measuring points in the undeformed and deformed state with respect to the centroids:

$$\widehat{\mathbf{p}}_{init,i} = \mathbf{p}_{init,i} - \overline{\mathbf{p}}_{init}, \quad \widehat{\mathbf{p}}_{def,i} = \mathbf{p}_{init,i} + \mathbf{\Delta p}_i - \overline{\mathbf{p}}_{def}, \quad i = 1,2,\ldots,k \tag{B.3}$$

3. By using the definitions in Eq. (B.3), reformulate the problem in Eq. (B.1) independent of **t**:

$$\mathbf{F} = \underset{\mathbf{F}\in\mathbb{R}^{2\times2}}{\operatorname{argmin}} \sum_{i=1}^{n} w_i \left\| \mathbf{F}\widehat{\mathbf{p}}_{init,i} - \widehat{\mathbf{p}}_{def,i} \right\|^2 \tag{B.4}$$

Eq. (B.4) now denotes a unconstrained weighted least-square problem with an explicit solution shown in the next step.

4. Compute the best-fit deformation gradient tensor:

$$\mathbf{F} = \widehat{\mathbf{P}}_{def}\mathbf{W}\widehat{\mathbf{P}}_{init}^{T}\left(\widehat{\mathbf{P}}_{init}\mathbf{W}\widehat{\mathbf{P}}_{init}^{T}\right)^{-1} \tag{B.5}$$

where $\widehat{\mathbf{P}}_{init} = \left[\widehat{\mathbf{p}}_{init,1},\ldots,\widehat{\mathbf{p}}_{init,k}\right]$ and $\widehat{\mathbf{P}}_{def} = \left[\widehat{\mathbf{p}}_{def,1},\ldots,\widehat{\mathbf{p}}_{def,k}\right]$ are matrices containing the centred positions of the measuring points in the undeformed and deformed state as their columns, respectively, and $\mathbf{W} = \operatorname{diag}(w_1,\ldots,w_k)$ is a $k \times k$ diagonal matrix with weights w_j on diagonal entry j.

5. Compute the best-fit translation:

$$\mathbf{t} = \overline{\mathbf{p}}_{def} - \mathbf{F}\overline{\mathbf{p}}_{init} \tag{B.6}$$

Appendix C

This appendix contains information on the Digital Image Correlation (DIC) and Automated Crack Detection and Measurement (ACDM) configurations as well as on the crack kinematic measurement uncertainty of the three experiments analysed in the study.

See Table C.1.

Table C.1
DIC and ACDM configuration of CTC-7, PT-1 and SL-1, including the uncertainty of the crack kinematic measurement.

		CTC-7 [40]	PT-1 [18]	SL-1 [11]
DIC configuration				
Avg. px/mm	[-]	2.17	2.67	2.51
Subset size *ss*	[px]	15	23	23
Step size *st*	[px]	2	3	3
Filter size *f*	[-]	5	7	5
Uncertainty of strains[1]	[1/1000]	1.0	0.7	0.7
ACDM configuration				
$T_{e1,inf}$	[1/1000]	1	1	1
$T_{e1,sup}$	[1/1000]	4	4	4
iw	[-]	9	9	9
$d_1 = d_{1,opt}$	[px]	22.63	33.94	33.94
$d_2 = d_{2,opt}$	[px]	11.31	16.97	16.97
$r_{RMS,ZST}$	[μm]	1.701	1.418	1.147
Ratio of reliable crack kinematic measurements that fulfil $r_i \leqslant T_r = 2r_{RMS,ZST}$				
Zero Strain Test (ZST)	[-]	0.996	0.970	0.965
Experiment (EXP)	[-]	0.974	0.709	0.686

[1] Quantified by the spatial standard deviation parameter obtained from the ZST, according to [8].

References

[1] Presvyri S, Yang Y, Hendriks M, Visser J, Hordijk D. On the extension of Walraven's aggregate interlock model based on laser scanned crack surface. In: Derkowski W, Krajewski P, Gwozdziewicz P, Pantak M, Hojdys L, editors. Proceedings of the Fib Symposium 2019. International Federation for Structural Concrete (fib); 2019. p. 937–44.

[2] Kaufmann W, Mata-Falcón J, Amin A. Compression Field Analysis of Fiber-Reinforced Concrete Based on the Cracked Membrane Model. Structural Journal 2019;116:213–24. https://doi.org/10.14359/51716763.

[3] Kaufmann W, Marti P. Structural Concrete: Cracked Membrane Model. Journal of Structural Engineering, ASCE 1998;124:1467–75. https://doi.org/10.1061/(ASCE)0733-9445(1998)124:12(1467).

[4] Kaufmann W. Strength and Deformations of Structural Concrete Subjected to In-Plane Shear and Normal Forces, Doctoral dissertation, Institut für Baustatik und Konstruktion. ETH Zürich 1998. https://doi.org/10.1007/978-3-0348-7612-4.

[5] Vecchio FJ, Collins MP. The Modified Compression-Field Theory for Reinforced Concrete Elements Subjected to Shear. ACI Journal Proceedings 1986;83:219–31. https://doi.org/10.14359/10416.

[6] Vecchio FJ. Disturbed Stress Field Model for Reinforced Concrete: Formulation. Journal of Structural Engineering, ASCE 2000;126:1070–7. https://doi.org/10.1061/(ASCE)0733-9445(2000)126:9(1070).

[7] Bentz EC, Vecchio FJ, Collins MP. Simplified Modified Compression Field Theory for Calculating Shear Strength of Reinforced Concrete Elements. ACI Structural Journal 2006;103:614–24. https://doi.org/10.14359/16438.

[8] Mata-Falcón J, Haefliger S, Lee M, Galkovski T, Gehri N. Combined application of distributed fibre optical and digital image correlation measurements to structural concrete experiments. Engineering Structures 2020;225:111309. https://doi.org/10.1016/j.engstruct.2020.111309.

[9] Kaufmann W, Mata Falcon J, Beck A. Future directions for research on shear in structural concrete, in: Towards a Rational Understanding of Shear in Beams and Slabs. International Federation for Structural Concrete(fib) 2018:323–38. https://www.research-collection.ethz.ch/handle/20.500.11850/281964.

[10] Gehri N, Mata-Falcón J, Kaufmann W. Automated crack detection and measurement based on digital image correlation. Construction and Building Materials 2020;256:119383. https://doi.org/10.1016/j.conbuildmat.2020.119383.

[11] Beck A. Paradigms of shear in structural concrete: Theoretical and experimental investigation, Doctoral Thesis. ETH Zurich 2021. https://doi.org/10.3929/ethz-b-000482684.

[12] Karagiannis D. Effect of transverse bending on the shear capacity of concrete bridges, Doctoral Thesis. ETH Zurich 2021. https://doi.org/10.3929/ethz-b-000485497.

[13] Gebhard L, Mata-Falcón J, Anton A, Dillenburger B, Kaufmann W. Experimental investigation of reinforcement strategies for concrete extrusion 3D printed beams, in. Proceeding of the 13th Fib International PhD-Symposium In Civil Engineering, Fédéération de l'Industrie du Béton(fib). 2020.

[14] Gebhard L, Mata-Falcón J, Anton A, Dillenburger B, Kaufmann W. Structural behaviour of 3D printed concrete beams with various reinforcement strategies. Engineering Structures 2021;240:112380. https://doi.org/10.1016/j.engstruct.2021.112380.

[15] Lee M, Mata Falcon J, Kaufmann W. Load-deformation behaviour of concrete tension ties with weft-knitted textile reinforcement, in. In: Proceedings of the 2020 Session of the 13th Fib International PhD Symposium in Civil Engineering, Fédération Internationale du Béton(fib); 2020. p. 70–7. https://doi.org/10.3929/ethz-b-000438439.

[16] Hoult R, Beyer K. RC U-shaped walls subjected to in-plane, diagonal, and torsional loading: New experimental findings. Engineering Structures 2021;233:111873. https://doi.org/10.1016/j.engstruct.2021.111873.

[17] Czaderski C, Shahverdi M, Michels J. Iron based shape memory alloys as shear reinforcement for bridge girders. Construction and Building Materials 2021;274:121793. https://doi.org/10.1016/j.conbuildmat.2020.121793.

[18] Kaufmann W, Beck A, Karagiannis D, Werne D. The Large Universal Shell Element Tester LUSET. ETH Zurich, Zurich: Institute of Structural Engineering; 2019.

[19] Morice PB, Base GD. The design and use of a demountable mechanical strain gauge for concrete structures. Magazine of Concrete Research 1953;5:37–42. https://doi.org/10.1680/macr.1953.5.13.37.

[20] Walraven JC. Aggregate interlock: A theoretical and experimental analysis, Doctoral dissertation. Delft University; 1980.

[21] Li B, Maekawa K, Okamura H. Contact density model for stress transfer across cracks in concrete. Journal of the Faculty of Engineering, The University of Tokyo 1989;40:9–52.

[22] T. Paulay, P.J. Loeber, Shear Transfer by Aggregate Interlock, ACI Special Publication. SP-42(1974) 1–16.

[23] A. Giraldo Soto, W. Kaufmann, Effect of Test Setups on the Shear Transfer Capacity Across Cracks in FRC, in: P. Serna, A. Llano-Torre, J.R. Martí-Vargas, J. Navarro-Gregori(Eds.), Fibre Reinforced Concrete: Improvements and Innovations, Springer International Publishing, Cham, 2021: pp. 163–175. Doi: 10.1007/978-3-030-58482-5_15.

[24] Cavagnis F, Fernández Ruiz M, Muttoni A. Shear failures in reinforced concrete members without transverse reinforcement: An analysis of the critical shear crack development on the basis of test results. Eng Struct 2015;103:157–73. https://doi.org/10.1016/j.engstruct.2015.09.015.

[25] Cavagnis F, Ruiz MF, Muttoni A. An analysis of the shear-transfer actions in reinforced concrete members without transverse reinforcement based on refined experimental measurements. Struct Concrete 2017:1–16. https://doi.org/10.1002/suco.201700145.

[26] Iliopoulos S, Aggelis DG, Pyl L, Vantomme J, Van Marcke P, Coppens E, et al. Detection and evaluation of cracks in the concrete buffer of the Belgian Nuclear Waste container using combined NDT techniques. Constr Build Mater 2015;78:369–78. https://doi.org/10.1016/j.conbuildmat.2014.12.036.

[27] Huber P, Huber T, Kollegger J. Investigation of the shear behavior of RC beams on the basis of measured crack kinematics. Eng Struct 2016;113:41–58. https://doi.org/10.1016/j.engstruct.2016.01.025.

[28] Küntz M, Jolin M, Bastien J, Perez F, Hild F. Digital image correlation analysis of crack behavior in a reinforced concrete beam during a load test. Can. J. Civ. Eng. 2006;33:1418–25. https://doi.org/10.1139/l06-106.

[29] Lecompte D, Vantomme J, Sol H. Crack Detection in a Concrete Beam using Two Different Camera Techniques. Struct Health Monitoring 2006;5:59–68. https://doi.org/10.1177/1475921706057982.

[30] Alam SY, Loukili A, Grondin F. Monitoring size effect on crack opening in concrete by digital image correlation, European Journal of Environmental and Civil. Engineering. 2012;16:818–36. https://doi.org/10.1080/19648189.2012.672211.

[31] Alam SY, Loukili A, Grondin F, Rozière E. Use of the digital image correlation and acoustic emission technique to study the effect of structural size on cracking of reinforced concrete. Eng Fract Mech 2015;143:17–31. https://doi.org/10.1016/j.engfracmech.2015.06.038.

[32] Muller M, Toussaint E, Destrebecq J-F, Grédiac M. Experimental and numerical study of reinforced concrete specimens strengthened with composite plates. Compos A Appl Sci Manuf 2004;35:885–93. https://doi.org/10.1016/j.compositesa.2004.01.009.

[33] Destrebecq J-F, Toussaint E, Ferrier E. Analysis of Cracks and Deformations in a Full Scale Reinforced Concrete Beam Using a Digital Image Correlation Technique. Exp Mech 2011;51:879–90. https://doi.org/10.1007/s11340-010-9384-9.

[34] Hoult NA, Dutton M, Hoag A, Take WA. Measuring Crack Movement in Reinforced Concrete Using Digital Image Correlation: Overview and Application to Shear Slip Measurements. Proc IEEE 2016;104:1561–74. https://doi.org/10.1109/JPROC.2016.2535157.

[35] Poldon JJ, Hoult NA, Bentz EC. Distributed Sensing in Large Reinforced Concrete Shear Test. SJ. 2019;116:235–45. https://doi.org/10.14359/51716765.

[36] Poldon J, Bentz E, Hoult N. Measuring and modelling shear crack widths and slips in a shear test of a member with stirrups. In: Proceedings of the Fib Symposium 2019: Concrete - Innovations in Materials, Design and Structures; 2019. p. 1858–65.

[37] Mündecke E, Mechtcherine V. Tensile behaviour of strain-hardening cement-based composites(SHCC) with steel reinforcing bars. Cem Concr Compos 2019:103423. https://doi.org/10.1016/j.cemconcomp.2019.103423.

[38] Ruocci G, Rospars C, Bisch P, Erlicher S, Moreau G. Cracks distance and width in reinforced concrete membranes: experimental results from cyclic loading histories. In: 15th World Conference on Earthquake Engineering, Lisbon, Portugal, 2012: pp. 1278–1284.

[39] Ruocci G, Rospars C, Moreau G, Bisch P, Erlicher S, Delaplace A, et al. Digital Image Correlation and Noise-filtering Approach for the Cracking Assessment of Massive Reinforced Concrete Structures. Strain 2016;52:503–21. https://doi.org/10.1111/str.12192.

[40] Wirion C. Load carrying and deformation capacity of concrete tension members and retaining walls with locally corroded reinforcement, Master's thesis. ETH Zürich 2019.

[41] Canny J. A Computational Approach to Edge Detection. In: IEEE Transactions on Pattern Analysis and Machine Intelligence. PAMI-8(1986) 679–698. Doi: 10.1109/TPAMI.1986.4767851.

[42] Correlated Solutions, Vic-3D Software Manual, Correlated Solutions Inc., 2019. http://www.correlatedsolutions.com/supportcontent/VIC-3D-8-Manual.pdf.

[43] Campana S, Fernández Ruiz M, Anastasi A, Muttoni A. Analysis of shear-transfer actions on one-way RC members based on measured cracking pattern and failure kinematics. Mag Concr Res 2013;65:386–404. https://doi.org/10.1680/macr.12.00142.

[44] Sorkine-Hornung O, Rabinovich M. Least-Squares Rigid Motion Using SVD 2016.

[45] Gambarova P, Karakoç C. A new approach to the analysis of the confinement role in regularly cracked concrete elements. In: International Association for Structural Mechanics in Reactor Technology(Ed.), Transactions of the 7th International Conference on Structural Mechanics in Reactor Technology, Chicago, Illinois, U.S. A., August 22 - 26, 1983. Vol. M: Reliability and Risk Analysis of Nuclear Power Plants, North-Holland Physics Publ, Amsterdam, 1983: pp. 251–261.

[46] Walraven JC. Fundamental Analysis of Aggregate Interlock. J Struct Division, ASCE 1981;107:2245–70.

[47] Zar JH. Biostatistical Analysis. 4th ed. Upper Saddle River, N.J.: Prentice Hall; 1998.

[48] Batschelet E. Circular statistics in biology., Academic Press, 111 Fifth Ave., New York, NY 10003, 1981, 388.(1981).

[49] Taylor CC. Automatic bandwidth selection for circular density estimation. Comput Stat Data Anal 2008;52:3493–500.

[50] Rots JG. Computational modeling of concrete fracture, Doctoral thesis, TU Delft, 1988. http://resolver.tudelft.nl/uuid:06985d0d-1230-4a08-924a-2553a171f08f (accessed February 26, 2019).
[51] Beck A, Gehri N, Mata-Falcón J, Kaufmann W. Cracked Membrane Model with Fixed, Interlocked Cracks: Numerical Implementation and Validation. J Struct Eng 2020;146:04019193. https://doi.org/10.1061/(ASCE)ST.1943-541X.0002461.
[52] Gower JC, Dijksterhuis GB. Procrustes problems. Oxford, UK: Oxford University Press; 2004. http://www.oup.com/uk/catalogue/?ci=9780198510581(accessed June 9, 2021).
[53] Gower J. Procrustes rotation problems. Math Scientist 1976;I:12–5.